An extended finite element method with smooth nodal stress

X. Peng[1], S. Kulasegaram[1], S. P. A. Bordas[1], and S. C. Wu[2]

[1]Institute of Mechanics and Advanced Materials, Cardiff University, Cardiff, CF24 3AA, UK
[2]State Key Laboratory of Traction Power, Southwest Jiaotong University, Chengdu, 610031, China

ABSTRACT

In this paper, we present a method to achieve smooth nodal stresses in the XFEM application. This method was developed by borrowing the ideas from the 'twice interpolating approximations' (TFEM) by Zheng *et al* (2011). The salient feature of the method is to introduce an 'average' gradient into the construction of the approximation, resulting in improved solution accuracy, both in the vicinity of the crack tip and in the far field. Due to the higher-order polynomial basis provided by the interpolants, the new approximation enhances the smoothness of the solution without requiring an increased number of degrees of freedom. This is particularly advantageous for low-order elements and in fracture mechanics. Since the new approach adopts the same mesh discretization, i.e. simplex meshes, it can be easily extended to various problems and is easily implemented. We also discuss the increased bandwidth which is a major drawback of the present method. Numerical tests show that the new method is as robust as the XFEM, considering precision, model size and post-processing time. By comparing the results from the present method with the XFEM for crack propagation in homogeneous material, we conclude that for two-dimensional problems, the proposed method tends to be an efficient alternative to the classical XFEM.
Keywords: *Double-interpolation approximation; higher-order element; smooth nodal stress; extended finite element method; crack propagation.*

1 Introduction

The extended finite element method (XFEM)[1] is a versatile and accurate approach to model strong discontinuities and singularities that exist in the problems of linear elastic fracture mechanics. In the XFEM, the approximation of the displacement field is decomposed by a regular part and an additional part (enrichment part) where the local partition of unity is applied [2]. The enrichment part allows to carry the specific information of the solution such as the discontinuity or singularity, through the additional degrees of freedom (DOFs) associated with the nodes in the variational formulation. This provides great flexibility to model cracks since alignment of the mesh and cracks is unnecessary when compared to the traditional FEM. Especially in terms of crack propagation, the modeling procedure is simplified since the remeshing operation is no longer needed, which is computationally expensive and tends to be cumbersome in analyzing nonlinear problems when the mapping of the internal variables is required. The XFEM for fracture has achieved substantial developments over past decades in 3D implementation [3][4][5], nonlinear problems [6][7] and dynamics problems [8], and has been utilized for

assessing the damage tolerance of complex structures in industrial applications [9]. Posteriori error indicators were proposed by Bordas and Duflot [10][11] due to the non-smoothness of the stress field in the XFEM. The C++ libraries [12] as well as the commercial packages [13][14] were developed for the XFEM. A close cousin of the XFEM called generalized finite element method (GFEM), was also proposed and applied for crack modeling [15].

We start by reviewing some of the most salient and recent advance in enriched finite elements. Significant effort has been expanded towards improving the accuracy and robustness of this method. In the standard XFEM, the local partition of unity is adopted, which means only certain nodes are enriched. This will result in some elements (the blending element) consisting of both regular and enriched nodes which do not conform to partition of unity. The existence of blending elements would lead to low accuracy. Chessa *et al* [16] developed an enhanced strain formulation which led to a good performance of local partition of unity enrichments [17]. Gracie *et al* [18] proposed the discontinuous Galerkin method aimed at eliminating the source of error in blending elements. More attempts can be referred from [19][20].

In terms of integration, the additional non-polynomial enriched functions in the approximation space make the quadrature of the stiffness matrix of enriched elements and blending elements more delicate. Meanwhile possible singularities, sharp gradients in the crack tip enrichment adds to the complexity for numerical integration. The traditional procedure to perform the integration is to sub-divide the enriched element and blending element into quadrature subcells to ensure the precision [1]. Ventura [21] proposed an approach to eliminate the quadrature subcells via replacing non-polynomial functions by 'equivalent' polynomials. But this method is only exact for triangular and tetrahedral elements. Another efficient integration scheme was proposed by transforming the domain integration into contour integration in [20]. Natarajan *et al* [22] developed a new numerical integration for arbitrary polygonal domains in 2D to compute stiffness matrix. In this method, each part of the elements that are cut or intersected by a discontinuity is conformally mapped onto a unit disc using Schwarz-Christoffel mapping. Thus sub-dividing procedure is avoided. More attempts were seen in smoothed XFEM, in which interior integration is transformed into boundary integration. Then sub-dividing become unnecessary [23]. Laborde *et al* [24] adopted the almost polar integration within the crack tip enriched element, which improves the convergence rate.

Another issue observed in the original version of XFEM is the non-optimal convergence rate. One improvement is to use geometrical enrichment [24], i.e., the enrichment of a set of nodes within a radial domain around the crack tip, and the whole dimension is independent of the mesh size. Nevertheless, this approach deteriorates the condition number of the stiffness matrix, which somewhat limits its application to 3D problems. In order to reduce the condition number, effective preconditioners were proposed by Béchet [25] and Menk *et al* [26].

Apart from XFEM which broadly aims at providing approximations which are tailed to the solution based on a priori knowledge about the solution, a number of interpolation methods have been developed in order to improve the efficiency of standard non-enriched FE methods. An example is the need for C^1 continuous approximation, for instance, to solve problem where continuity of the first derivative of the unknown primal field is required. This is the case for higher-order gradient models, such as gradient elasticity [27], Kirchhoff-love shell models [28]. Methods satisfying this need include mesh-based and mesh-free methods [29]. In terms of higher-order continuous FEM, Papanicolopulos and Zervos [30][31] created a series of triangular elements with C^1 continuous interpolation properties. Fischer *et al* [32] compared the performance of C^1 finite elements and the C^1 natural element method (NEM) applied to non-linear gradient elasticity. Various meshfree methods are introduced and used widely in engineerings problems. The element free Galerkin method (EFG) [33] adopts the moving least-squares interpolants to construct trial and test functions which can easily obtain higher continuous in both variable

and its gradient. One similar method is the reproducing kernel particle method (RKPM)[34]. The meshfree radial basis functions method (RBFs) utilizes the radial basis function to interpolate scattered nodal data and is employed with point interpolation method (PIM) by Liu *et al.* The radial PIM (RPIM)[35][36][37], consists of both radial basis and polynomial basis in the approximation, which can avoid the singularity of the moment matrix in polynomial basis. The maximum-entropy method (MAXENT) proposed by Arroyo and Oritiz bridges Delaunay triangulation and maximum-entropy statistical interface [38]. And its second order form can be applied to optimize the support size in meshfree methods [39]. Liu *et al* developed a smoothed FEM (SFEM) based on the generalization of the strain smoothing technique to functions in the G space [40]. According to different smoothing integration domain, the SFEM can be classified as node-based smoothed FEM (NSFEM) and edge-based smoothed FEM (ESFEM). Many researchers subsequently investigated the new methods into modelling discontinuities using the enriched form by applying partition of unity into these new methods, such as extended SFEM [23][41][42][43][44][45]or extended EFG [46].

In this paper, a new approximation, which is based on the simplex mesh discretization and has C^1 continuity on most nodes, is investigated. This approximation procedure shares the attractive features of XFEM and higher-order continuous approximations and we named it the extended double-interpolation FEM (XDFEM) due to the fact that two consecutive stages of interpolation are used in the construction of this approximation. The first stage of interpolation is performed by Lagrange interpolation to obtain nodal variables and nodal gradients. The problem field is reproduced in the latter interpolation using the nodal values and gradients derived from the previous interpolation. The re-constructed trial functions will maintain C^1 continuity at the nodes [47]. Cubic polynomials are contained in the space without increasing total DOFs. This feature enhances the ability of the method to reproduce the solution near the crack tip [48] and improves the accuracy per DOFs, The price to pay is increased computational expense per DOFs, as discussed later in the paper. Analogous to meshfree methods, the nodal stresses can be calculated in a straightforward manner without any post-processing.

The paper is organised as follows. In section 2, the unenriched formulation for 1D and 2D is systematically introduced with a example of 1D bar simulation. Section 3 presents the discretized formulation of the enriched version of the proposed approximation for linear elastic fracture mechanics. Several numerical examples are presented to illustrate the advantages and probable limitations of DFEM and XDFEM in section 4. Finally, in section 5, concluding remarks are made with pointers to possible future work.

2 The double-interpolation approximation

2.1 1D approximation by double-interpolation

The basic idea of the double-interpolation approximation is to interpolate the unknown fields, using both the primary nodal values and nodal gradients, which are generated by the finite element interpolation in simplex mesh discretization. The proposed 1D double-interpolation is comparable to Hermite interpolants. Figure 1 shows a 1D domain which is discretized by six 1D elements. For the point of interest x in element e_3, the numerical value of the displacement can be interpolated by

$$\forall x \in [0, \ell], \quad u^h(x) = \phi_I(x)u^I + \psi_I(x)u^I_{,x} + \phi_J(x)u^J + \psi_J(x)u^J_{,x}, \tag{1}$$

where $u^I, u^I_{,x}$ denote the nodal displacement and nodal derivative of the displacement field at node I, respectively. $\ell = x_j - x_i$ is the length of the element. $\phi_I, \psi_I, \phi_J, \psi_J$ are the cubic

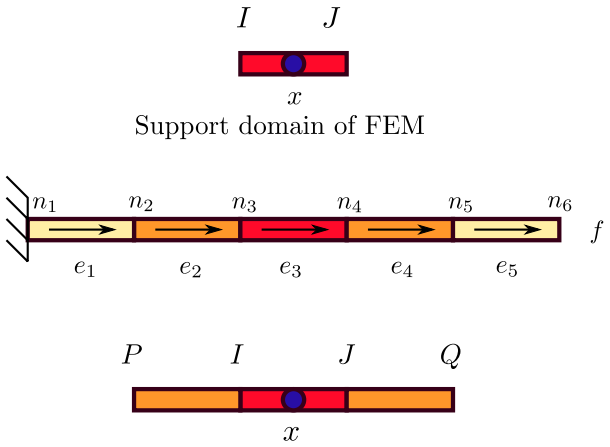

Figure 1: Discretization of the 1D domain and the element support domain of FEM and DFEM

Hermite basis polynomials given by:

$$\phi_I(x) = \left(1 + 2\left(\frac{x - x_I}{x_J - x_I}\right)\right)\left(\frac{x - x_J}{x_J - x_I}\right)^2, \tag{2a}$$

$$\psi_I(x) = (x - x_I)\left(\frac{x - x_J}{x_J - x_I}\right)^2, \tag{2b}$$

$$\phi_J(x) = \left(1 - 2\left(\frac{x - x_J}{x_J - x_I}\right)\right)\left(\frac{x - x_I}{x_J - x_I}\right)^2, \tag{2c}$$

$$\psi_J(x) = (x - x_J)\left(\frac{x - x_I}{x_J - x_I}\right)^2. \tag{2d}$$

We note that

$$\begin{aligned} \phi_I(\mathbf{x}_L) &= \delta_{IL}, \quad \phi_{I,x}(\mathbf{x}_L) = 0, \\ \psi_I(\mathbf{x}_L) &= 0 \quad , \quad \psi_{I,x}(\mathbf{x}_L) = \delta_{IL}, \end{aligned} \tag{3}$$

which guarantees the Dirichlet boundary conditions can be exactly applied in the second stage of interpolation. If we define the local coordinates as follows,

$$L_I(x) = \frac{x - x_J}{\ell}, \quad L_J(x) = -\frac{x - x_I}{\ell}, \tag{4}$$

then the Hermite basis polynomials can be written as:

$$\phi_I(x) = L_I(x) + (L_I(x))^2 L_J(x) - L_I(x)(L_J(x))^2, \tag{5a}$$

$$\psi_I(x) = \ell L_J(x)(L_I(x))^2, \tag{5b}$$

$$\phi_J(x) = L_J(x) + (L_J(x))^2 L_I(x) - L_J(x)(L_I(x))^2, \tag{5c}$$

$$\psi_J(x) = -\ell L_I(x)(L_J(x))^2. \tag{5d}$$

Subsequently, we will use the 'average' nodal gradients $(\bar{u}^I_{,x}, \bar{u}^J_{,x})$ derived from finite element interpolation at each node to replace the gradients $(u^I_{,x}, u^J_{,x})$ in Equation (1). But before we start calculating the average nodal gradients, an element set and a node set should be defined

which closely relate to the derivation. First of all, we put all the elements contained in the support domain[1]for a point of interest into the element set Λ. Then, all the support nodes for a point of interest are listed in the node set $\mathscr{N}$. For instance, in Figure 1, for the point of interest x inside element e_3, $\Lambda = \{e_3\}$ and $\mathscr{N} = \{n_3, n_4\}$ (or $\mathscr{N} = \{x_I, x_J\}$ in a local representation) for classical FEM. While for nodes on the element boundary, like n_3 (or x_I), $\Lambda_I = \{e_2, e_3\}$ and $\mathscr{N}_I = \{n_2, n_3, n_4\}$ (or $\mathscr{N}_I = \{x_P, x_I, x_J\}$) for classical FEM. Now Equation (1) can be rewritten as:

$$u^h(x) = \phi_I(x)u^I + \psi_I(x)\bar{u}^I_{,x} + \phi_J(x)u^J + \psi_J(x)\bar{u}^J_{,x}, \tag{6}$$

where

$$u^I = u(x_I) = N^{e_3}_I(x_I)u^I + N^{e_3}_J(x_I)u^J, \tag{7}$$

$$\bar{u}^I_{,x} = \bar{u}_{,x}(x_I) = \omega_{e_{2,I}}u^{e_2}_{,x}(x_I) + \omega_{e_{3,I}}u^{e_3}_{,x}(x_I), \tag{8}$$

in which $N^{e_3}_I$, $N^{e_3}_J$ are linear finite element shape functions. In order to emphasis the support domain of FEM, the element number is used as the superscript of the shape functions. This means in Equation (7), the displacement at x_I (or n_3) is interpolated in the element of interest e_3, although $N^{e_3}_J(x_I) = 0$, we still add this term in order for a clear derivation. $u^{e_2}_{,x}(x_I)$ is the nodal derivative at x_I calculated in element e_2, which belongs to Λ_I, the support element set of x_I. $\omega_{e_{2,I}}$ denotes the weight of element e_2 in Λ_I. These parameters are calculated by:

$$u^{e_2}_{,x}(x_I) = N^{e_2}_{P,x}(x_I)u^P + N^{e_2}_{I,x}(x_I)u^I, \tag{9}$$

$$\omega_{e_{2,I}} = \frac{meas(e_{2,I})}{meas(e_{2,I}) + meas(e_{3,I})}, \tag{10}$$

where $N^{e_2}_{P,x}(x), N^{e_2}_{I,x}(x)$ are the derivatives of the corresponded shape functions associated with element e_2. $meas(\cdot)$ denotes the length of the 1D element.

Substituting equations (10) and (9), into Equation (8) yields:

$$\begin{aligned}\bar{u}^I_{,x} = \bar{u}_{,x}(x_I) =& \omega_{e_{2,I}}\left(N^{e_2}_{P,x}(x_I)u^P + N^{e_2}_{I,x}(x_I)u^I\right) + \\ & \omega_{e_{3,I}}\left(N^{e_3}_{I,x}(x_I)u^I + N^{e_3}_{J,x}(x_I)u^J\right),\end{aligned} \tag{11}$$

which can be rewritten as:

$$\bar{u}^I_{,x} = \begin{bmatrix} \omega_{e_{2,I}}N^{e_2}_{P,x} & \omega_{e_{2,I}}N^{e_2}_{I,x} + \omega_{e_{3,I}}N^{e_3}_{I,x} & \omega_{e_{3,I}}N^{e_3}_{J,x} \end{bmatrix} \begin{bmatrix} u^P \\ u^I \\ u^J \end{bmatrix}. \tag{12}$$

By defining,

$$\bar{N}_{L,x}(x_I) = \sum_{e_i \in \Lambda_I} \omega_{e_{i,I}}N^{e_i}_{L,x}(x_I), \quad L \in \mathscr{N}_I, \tag{13}$$

the averaged derivative at node x_I can be written as

$$\bar{u}^I_{,x} = \bar{u}_{,x}(x_I) = \bar{N}_{P,x}(x_I)u^P + \bar{N}_{I,x}(x_I)u^I + \bar{N}_{J,x}(x_I)u^J. \tag{14}$$

Now, substituting Equations (7) and (14) into (6) results in:

[1]Support domain means the field for the point of interest x in an element, where the shape functions are non-zero at x.

$$
\begin{aligned}
u^h(x) =& \phi_I(x)\left(N_I(x_I)u^I + N_J(x_I)u^J\right) + \\
& \psi_I(x)\left(\bar{N}_{P,x}(x_I)u^P + \bar{N}_{I,x}(x_I)u^I + \bar{N}_{J,x}(x_I)u^J\right) + \\
& \phi_J(x)\left(N_I(x_J)u^I + N_J(x_J)u^J\right) + \\
& \psi_J(x)\left(\bar{N}_{I,x}(x_J)u^I + \bar{N}_{J,x}(x_J)u^J + \bar{N}_{Q,x}(x_J)u^Q\right) \\
=& \psi_I(x)\bar{N}_{P,x}(x_I)u^P + \\
& \left(\phi_I(x)N_I(x_I) + \psi_I(x)\bar{N}_{I,x}(x_I) + \phi_J(x)N_I(x_J) + \psi_J(x)\bar{N}_{I,x}(x_J)\right)u^I + \\
& \left(\phi_I(x)N_J(x_I) + \psi_I(x)\bar{N}_{J,x}(x_I) + \phi_J(x)N_J(x_J) + \psi_J(x)\bar{N}_{J,x}(x_J)\right)u^J + \\
& \psi_J(x)\bar{N}_{Q,x}(x_J)u^Q.
\end{aligned}
\tag{15}
$$

Hence, by defining,

$$
\hat{N}_L(x) = \phi_I(x)N_L(x_I) + \psi_I(x)\bar{N}_{L,x}(x_I) + \phi_J(x)N_L(x_J) + \psi_J(x)\bar{N}_{L,x}(x_J), \tag{16}
$$

the final form for the double-interpolation approximation can be obtained as:

$$
u^h(x) = \sum_{L\in\hat{\mathscr{N}}} \hat{N}_L(x)u^L, \tag{17}
$$

in which $\hat{\mathscr{N}}$ denotes the support node set for the point of interest x in DFEM. We also use $\hat{\Lambda}$ as the the support element set in DFEM. Thus, for the point of interest x, $\hat{\Lambda} = \Lambda_I \cup \Lambda_J = \{e_2, e_3, e_4\}$, $\hat{\mathscr{N}} = \mathscr{N}_I \cup \mathscr{N}_J = \{n_2, n_3, n_4, n_5\}$ (or $\hat{\mathscr{N}} = \{x_P, x_I, x_J, x_Q\}$ in the local representation as presented in Figure 1). Due to the computation of $\bar{u}^I_{,x}$ and $\bar{u}^J_{,x}$, the support domain of point of interest x in e_3 has been expanded in DFEM approximation. Similarly, the support domain of element boundary node n_3 (or x_I) is also expended in DFEM, i.e., $\hat{\Lambda}_I = \{e_1, e_2, e_3, e_4\}$ and $\hat{\mathscr{N}}_I = \{n_1, n_2, n_3, n_4, n_5\}$. It can be observed that derivative interpolants have already been embedded in Equation 17. we can also infer that due to the enlargement of the local support domain, DFEM will result in an increased bandwidth, thus have an increased computational cost per DOFs, but this is essential to construct the C^1 interpolants. Figure 2 shows the DFEM shape function and derivative at node n_3.

To more clearly depict the behavior of the proposed method, a numerical example is considered in the following discussion. For this purpose a 1D bar (as illustrated in Figure 1) problem is solved using both DFEM and FEM. The equilibrium equation for the 1D problem is defined as:

$$
EA\frac{\mathrm{d}^2u}{\mathrm{d}x^2} + f = 0, \tag{18a}
$$

$$
\epsilon(x) = u_{,x}(x), \tag{18b}
$$

$$
\sigma(x) = E\epsilon_{,x}(x), \tag{18c}
$$

$$
u|_{x=0} = 0, \tag{18d}
$$

where f is a uniform body force applied to the 1D bar. The exact solution for the displacement and stress are given by:

$$
u(x) = \frac{fL^2}{EA}\left(\frac{x}{L} - \frac{1}{2}\left(\frac{x}{L}\right)^2\right), \tag{19a}
$$

$$
\sigma(x) = \frac{fL}{A}\left(1 - \frac{x}{L}\right), \tag{19b}
$$

where L, A and E are the total length, area of the cross section and Young's Modulus respectively. For simplicity, all these parameters are assumed to have unit value in the simulation.

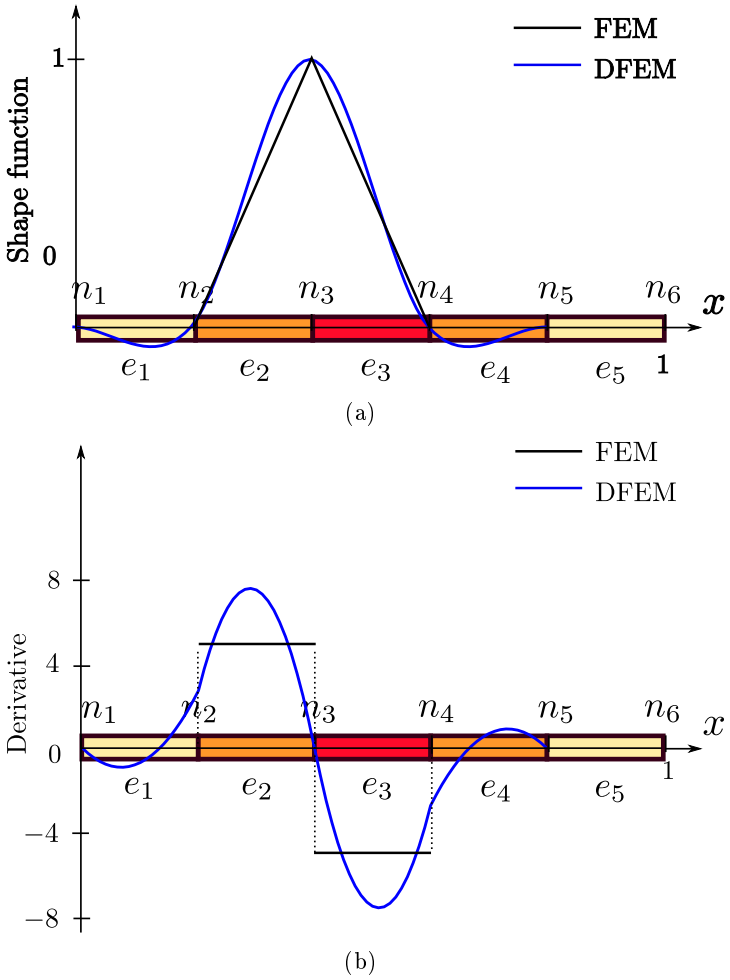

Figure 2: The 1D DFEM shape function and its derivative at node 3

Figure 3 compares the displacement and stress values obtained by both FEM and DFEM. It can be observed from the figure that DFEM capture the exact solution much better than the piecewise linear curve obtained by the FEM for the displacement field. In addition, apart from the end or boundary points, the numerical results of DFEM for stress distribution agrees well with the exact solution. The deterioration of the DFEM solution near the boundary nodes are attributed to the automatic recover of the calculation of nodal gradients at the end points, which will be explained in the following section. Figure 4 plots the relative error in the displacement and energy norm of the 1D bar problem (The definitions of these norms can be referred from section 4). It is clearly illustrated that DFEM approximation in 1D can achieve a convergence rate between the linear and quadratic order.

2.2 2D approximation by double interpolation

As illustrated in Figure 5, $\mathbf{x} = (x, y)$ denotes the point of interest in triangle IJK. Analogous to the derivation procedure for 1D formulation, the 2D double-interpolation approximation in a mesh of triangular element can be given as follows:

$$\mathbf{u}^h(\mathbf{x}) = \sum_{L \in \hat{\mathcal{N}}} \hat{N}_L(\mathbf{x}) \mathbf{u}^L, \tag{20}$$

$$\begin{aligned} \hat{N}_L(\mathbf{x}) =& \phi_I(\mathbf{x}) N_L(\mathbf{x}_I) + \psi_I(\mathbf{x}) \bar{N}_{L,x}(\mathbf{x}_I) + \varphi_I(\mathbf{x}) \bar{N}_{L,y}(\mathbf{x}_I) + \\ & \phi_J(\mathbf{x}) N_L(\mathbf{x}_J) + \psi_J(\mathbf{x}) \bar{N}_{L,x}(\mathbf{x}_J) + \varphi_J(\mathbf{x}) \bar{N}_{L,y}(\mathbf{x}_J) + \\ & \phi_K(\mathbf{x}) N_L(\mathbf{x}_K) + \psi_K(\mathbf{x}) \bar{N}_{L,x}(\mathbf{x}_K) + \varphi_K(\mathbf{x}) \bar{N}_{L,y}(\mathbf{x}_K), \end{aligned} \tag{21}$$

where $\mathbf{u}^L$ is the nodal displacement vector. In the following discussion the evaluation of the average derivative of the shape function at node $\mathbf{x}_I$ is considered. The average derivative of the shape function at node $\mathbf{x}_I$ can be written as:

$$\bar{N}_{L,x}(\mathbf{x}_I) = \sum_{e_{i,I} \in \Lambda_I} \omega_{e_{i,I}} N^{e_i}_{L,x}(\mathbf{x}_I), \tag{22a}$$

$$\bar{N}_{L,y}(\mathbf{x}_I) = \sum_{e_{i,I} \in \Lambda_I} \omega_{e_{i,I}} N^{e_i}_{L,y}(\mathbf{x}_I), \tag{22b}$$

where $\omega_{e_{i,I}}$ is the weight of element e_i in Λ_I and is computed by:

$$\omega_{e_{i,I}} = meas(e_i) / \sum_{e_i \in \Lambda_I} meas(e_i). \tag{23}$$

Here $meas(\cdot)$ denotes the area of a triangular element. An example of how to evaluate the weight of an element is presented in Figure 5. ϕ_I, ψ_I and φ_I form the polynomial basis associated with $\mathbf{x}_I$, which satisfies the following interpolating conditions:

$$\begin{array}{lll} \phi_I(\mathbf{x}_L) = \delta_{IL}, & \phi_{I,x}(\mathbf{x}_L) = 0 \quad , & \phi_{I,y}(\mathbf{x}_L) = 0, \\ \psi_I(\mathbf{x}_L) = 0 \quad , & \psi_{I,x}(\mathbf{x}_L) = \delta_{IL}, & \psi_{I,y}(\mathbf{x}_L) = 0, \\ \varphi_I(\mathbf{x}_L) = 0 \quad , & \varphi_{I,x}(\mathbf{x}_L) = 0 \quad , & \varphi_{I,y}(\mathbf{x}_L) = \delta_{IL}. \end{array} \tag{24}$$

And these polynomial basis functions are given by:

$$\begin{aligned} \phi_I(\mathbf{x}) =& L_I(\mathbf{x}) + (L_I(\mathbf{x}))^2 L_J(\mathbf{x}) + (L_I(\mathbf{x}))^2 L_K(\mathbf{x}) \\ & - L_I(\mathbf{x}) (L_J(\mathbf{x}))^2 - L_I(\mathbf{x}) (L_K(\mathbf{x}))^2, \end{aligned} \tag{25a}$$

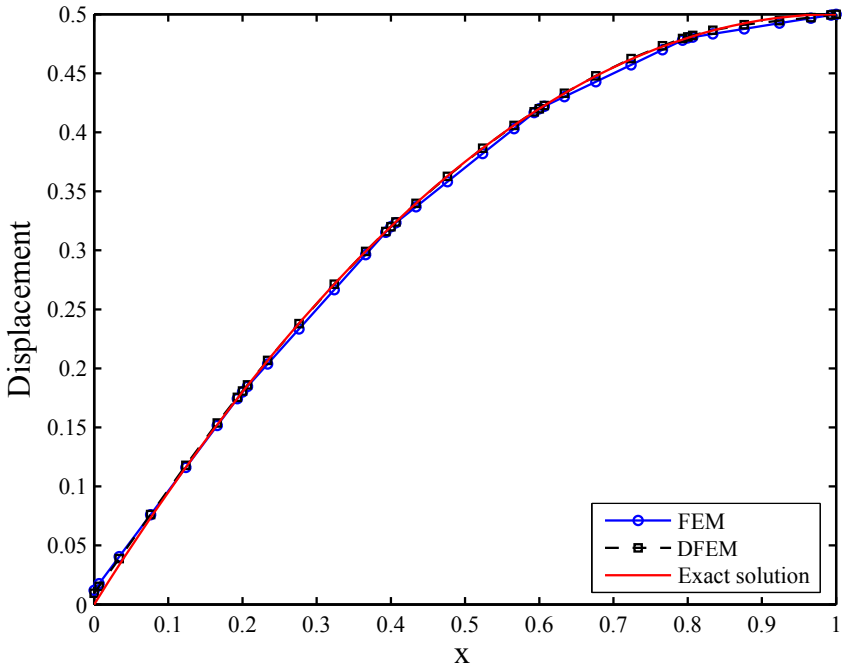

(a)

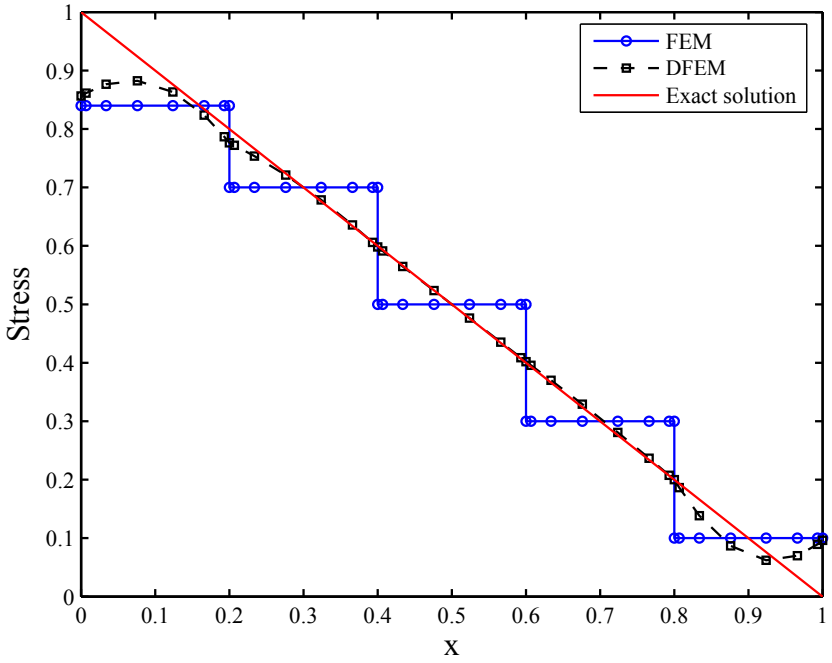

(b)

Figure 3: The comparison of FEM and DFEM results for 1D bar:(a)displacement;(b)stress

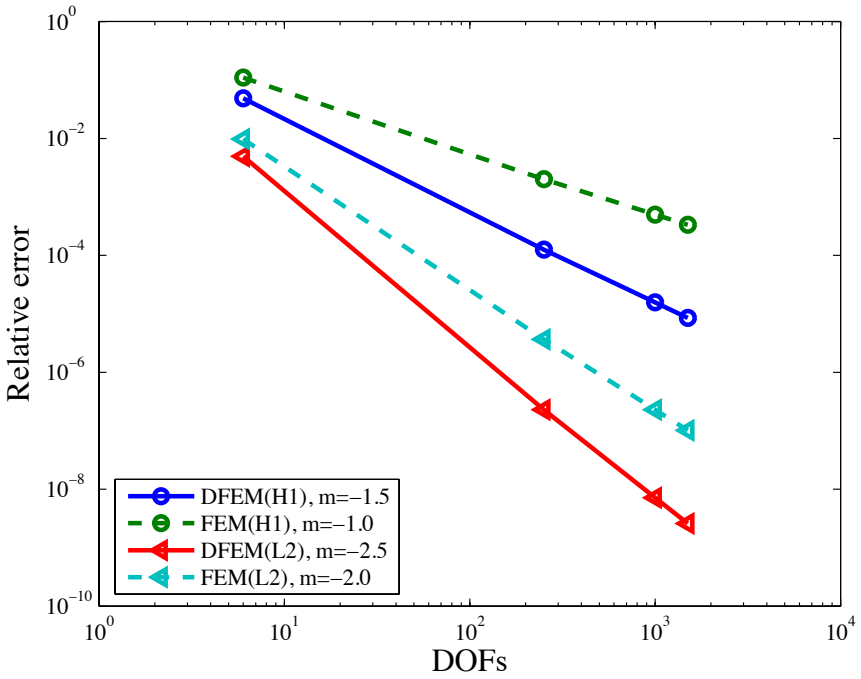

Figure 4: Relative error in displacement and energy norm of 1D bar

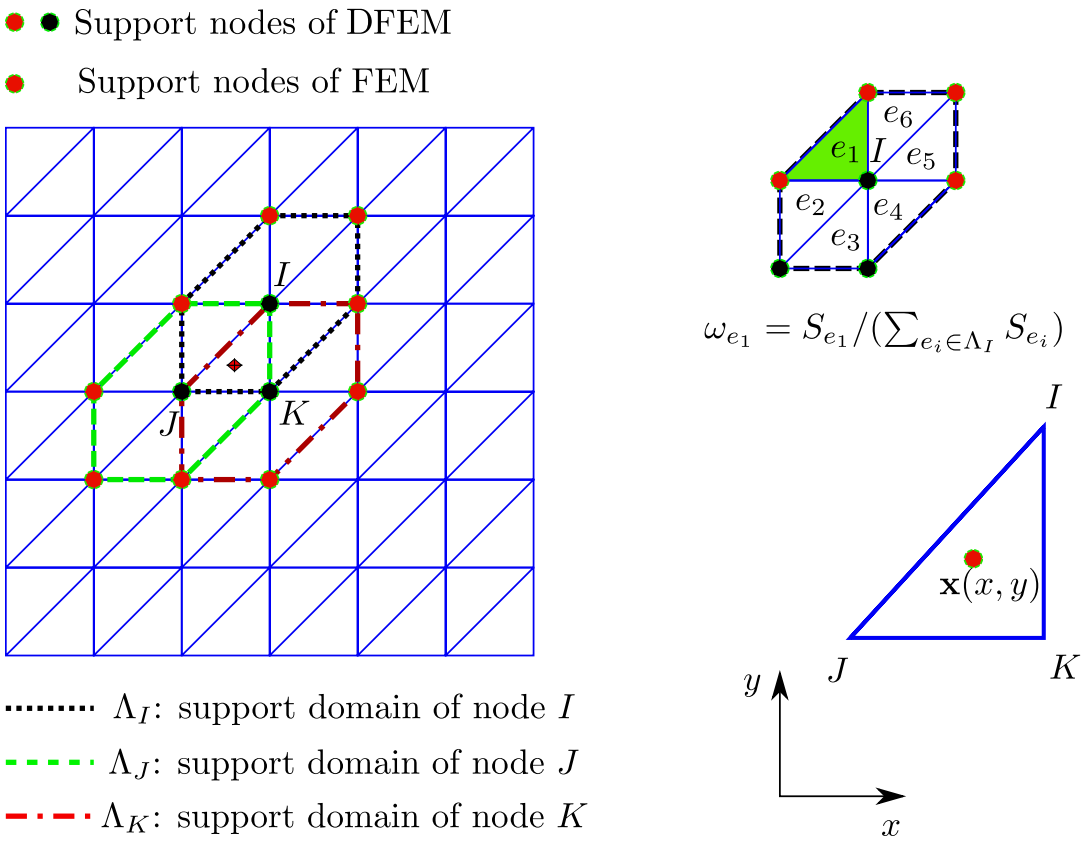

Figure 5: Illustration for the support domain of DFEM

$$\psi_I(\mathbf{x}) = -c_J\left(L_K(\mathbf{x})\left(L_I(\mathbf{x})\right)^2 + \frac{1}{2}L_I(\mathbf{x})L_J(\mathbf{x})L_K(\mathbf{x})\right) + c_K\left(\left(L_I(\mathbf{x})\right)^2 L_J(\mathbf{x}) + \frac{1}{2}L_I(\mathbf{x})L_J(\mathbf{x})L_K(\mathbf{x})\right), \tag{25b}$$

$$\varphi_I(\mathbf{x}) = b_J\left(L_K(\mathbf{x})\left(L_I(\mathbf{x})\right)^2 + \frac{1}{2}L_I(\mathbf{x})L_J(\mathbf{x})L_K(\mathbf{x})\right) - b_K\left(\left(L_I(\mathbf{x})\right)^2 L_J(\mathbf{x}) + \frac{1}{2}L_I(\mathbf{x})L_J(\mathbf{x})L_K(\mathbf{x})\right). \tag{25c}$$

Note that the polynomial basis functions $\phi_J, \psi_J, \varphi_J, \phi_K, \psi_K$ and φ_K can be obtained by the above definitions via cyclic permutation of indices I, J and K. In the above equations, $L_I(\mathbf{x}), L_J(\mathbf{x})$ and $L_K(\mathbf{x})$ are the area coordinates of the point of interest $\mathbf{x}$ in triangle IJK. For the point of interest $\mathbf{x}$ in Figure 5, the $L_I(\mathbf{x}), b_I$ and c_I are presented as follows.

$$L_I(\mathbf{x}) = \frac{1}{2\triangle}(a_I + b_I x + c_I y), \tag{26a}$$

$$a_I = x_J y_K - x_K y_J, \tag{26b}$$

$$b_I = y_J - y_K, \tag{26c}$$

$$c_I = x_K - x_J, \tag{26d}$$

where $\triangle$ is the area of triangle IJK. Further, L_J, L_K, b_J, b_K, c_J and c_K can be obtained using the above definitions via cyclic permutation of indices I, J and K.

When the point of interest lies on one of the edges, for example on edge IJ, the basis functions will boil down to 1D basis functions and will be consistent with the 1D form presented in the preceding section.

The DFEM shape functions posess the properties such as the linear completeness, partition of unity, the Dirac delta property [47]. In addition, the 2D DFEM possesses C^1 continuity at the nodes and C^0 continuity on edges. Compared to 3-noded triangular element, the DFEM basis functions can achieve a higher-order approximation without the introduction of additional nodes, which will be seen the numerical examples in next section. However, this attractive feature comes with the price of an increased bandwidth as the neighboring nodes are used to obtain the nodal gradients necessary for the second interpolation. The details of such computational costs will be discussed in the section devoted to numerical examples.

2.3 Modification of the nodal gradients

When C^0 continuity of the primal field at a node is needed, for instance on the nodes at material interface, it is useful to modify the calculation of the average nodal gradient as discussed below. The calculation of the nodal gradient can be performed as follows:

$$\bar{N}_{L,x}(\mathbf{x}_I) = N^e_{L,x}(\mathbf{x}_I). \tag{27}$$

The right hand side is the derivative of N_L computed in element e, in which the point of interest $\mathbf{x}$ is located. This is easily done in the implementation by replacing the average derivative with the derivative in the element of interest. It can be observed that nodes at the endpoint of a 1D bar automatically satisfy the above equation. All the topological enriched nodes in XFEM (the nodes circled by red boxes in Figure 7 and Figure 8) have been relaxed to C^0 as well due to the fact that during the average calculation of gradients in Equation (22), the contribution from split elements cannot be computed directly as from continuous elements in an area weighted way (Equation (23)) due to the discontinuity.

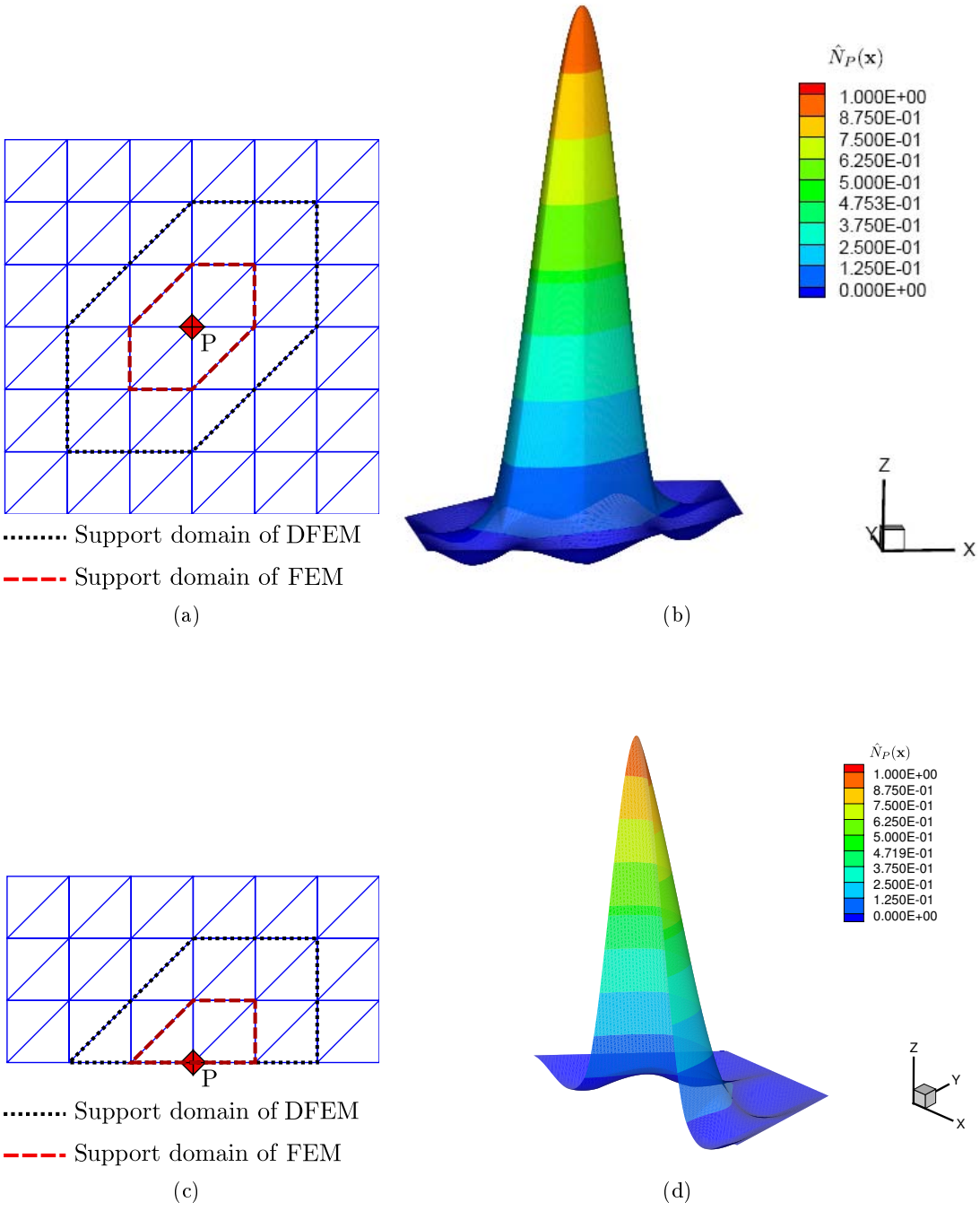

Figure 6: The shape functions of DFEM in 2D

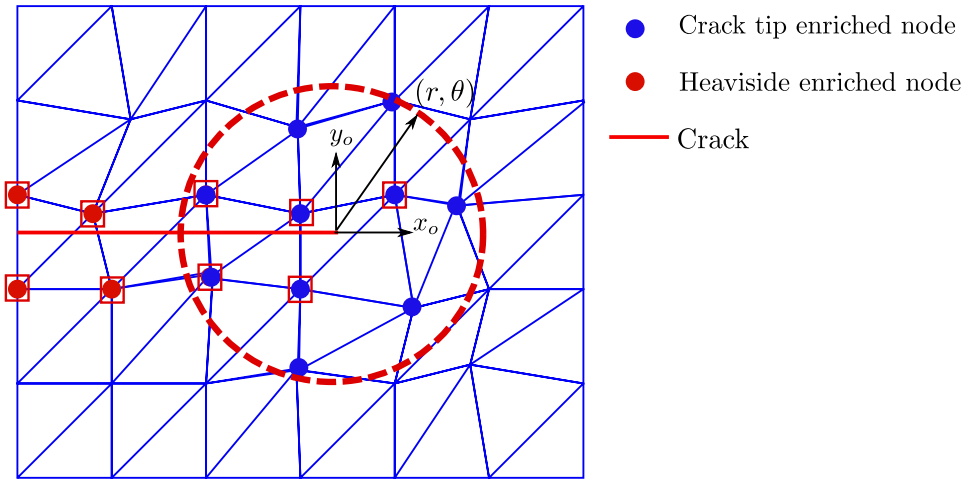

Figure 7: Nodal enrichment in XDFEM; the nodes encircled by red box are degenerated to C^0, see section 2.3

2.4 The enriched 2D double-interpolation approximation

The extended finite element method uses a partition of unity which allows for the addition of a priori knowledge about the solution of boundary value problems into the approximation space of the numerical solution. The crack can be described in XFEM by enriching the standard displacement approximation as follows:

$$\mathbf{u}^h(\mathbf{x}) = \sum_{I\in\mathcal{N}_I} \hat{N}_I(\mathbf{x})\mathbf{u}^I + \sum_{J\in\mathcal{N}_J} \hat{N}_J(\mathbf{x})H(\mathbf{x})\mathbf{a}^J + \sum_{K\in\mathcal{N}_K} \hat{N}_K(\mathbf{x}) \sum_{\alpha=1}^{4} f_\alpha(\mathbf{x})\mathbf{b}^{K\alpha}, \tag{28}$$

where $\mathbf{u}^I$ are the regular DOFs. $\mathbf{a}^J$ are the additional Heaviside enriched DOFs. $\mathbf{b}^{K\alpha}$ are the additional crack tip enriched DOFs. $\mathcal{N}_I$,$\mathcal{N}_J$ and $\mathcal{N}_K$ are the collections of regular non-enriched nodes, Heaviside enriched nodes and crack tip enriched nodes, respectively. $H(\cdot)$ is the Heaviside function. The crack tip enrichment functions are defined as:

$$\{f_\alpha(r,\theta), \alpha = 1,4\} = \left\{\sqrt{r}\sin\frac{\theta}{2}, \sqrt{r}\cos\frac{\theta}{2}, \sqrt{r}\sin\frac{\theta}{2}\sin\theta, \sqrt{r}\cos\frac{\theta}{2}\sin\theta\right\}, \tag{29}$$

where (r,θ) are the polar coordinates of the crack tip (Figure 7). Figure 9 compares the Heaviside enriched shape functions obtained with XFEM and XDFEM which are defined in Figure 8.

3 Weak form and discretized formulations

For an elastostatic body as in Figure 10 defined by Hooker's tensor $\mathbf{C}$ and undergoing small strains and small displacements, the equilibrium equations and boundary conditions for the Cauchy stress $\boldsymbol{\sigma}$ and the displacement field $\mathbf{u}$ write:

$$\begin{array}{ccc} \nabla\cdot\boldsymbol{\sigma} = \mathbf{0} & \text{on} & \Omega, \\ \boldsymbol{\sigma}\cdot\mathbf{n} = \bar{\mathbf{t}} & \text{on} & \Gamma_t, \\ \mathbf{u} = \bar{\mathbf{u}} & \text{on} & \Gamma_u. \end{array} \tag{30}$$

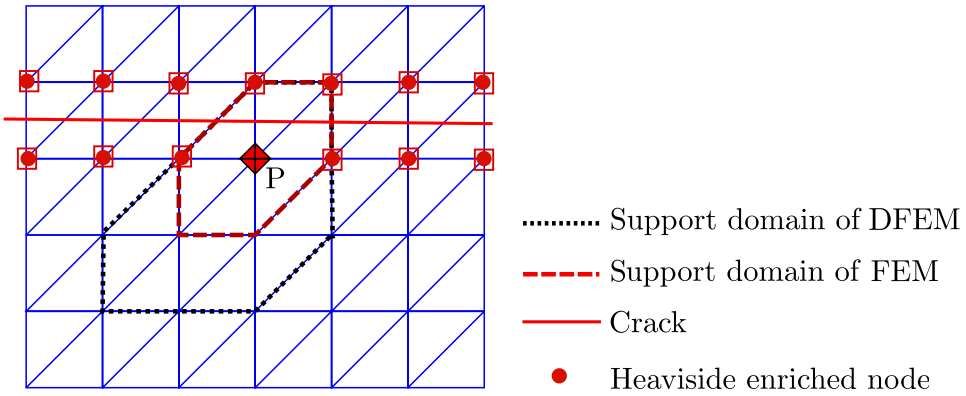

Figure 8: The support domain of enriched DFEM; the nodes encircled by red box are degenerated to C^0, see section 2.3

Here $\bar{\mathbf{t}}$ is the traction imposed on boundary Γ_t. Further, assuming traction free crack faces:

$$\boldsymbol{\sigma} \cdot \mathbf{n} = \mathbf{0} \qquad \text{on} \quad \Gamma_{c^+} \text{ and } \Gamma_{c^-}, \tag{31}$$

where $\Gamma_{c^+}, \Gamma_{c^-}$ are the upper and lower crack surfaces respectively. The strain-displacement relation and the constitutive law are respectively as:

$$\boldsymbol{\epsilon} = \frac{1}{2}\left(\nabla + \nabla^{\mathrm{T}}\right) \otimes \mathbf{u}, \tag{32a}$$

$$\boldsymbol{\sigma} = \mathbf{C} : \boldsymbol{\epsilon}. \tag{32b}$$

Using a Bubnov-Galerkin weighted residual formulation based on Lagrange test and trial spaces, substituting the trial and test functions into the weak form of Equation (30), and using the arbitrariness of nodal variations, the discretized equations can be written:

$$\mathbf{K}\mathbf{u} = \mathbf{f}, \tag{33}$$

where $\mathbf{u}$ is the nodal vector of the unknown displacements and $\mathbf{K}$ is the stiffness matrix. The elemental form of $\mathbf{K}$ for element e is given by:

$$\mathbf{K}_{IJ}^{e} = \begin{bmatrix} \mathbf{K}_{IJ}^{uu} & \mathbf{K}_{IJ}^{ua} & \mathbf{K}_{IJ}^{ub} \\ \mathbf{K}_{IJ}^{au} & \mathbf{K}_{IJ}^{aa} & \mathbf{K}_{IJ}^{ab} \\ \mathbf{K}_{IJ}^{bu} & \mathbf{K}_{IJ}^{ba} & \mathbf{K}_{IJ}^{bb} \end{bmatrix}. \tag{34}$$

The external force vector $\mathbf{f}$ is defined as

$$\mathbf{f}_I = \{\mathbf{f}_I^u \quad \mathbf{f}_I^a \quad \mathbf{f}_I^{b^1} \quad \mathbf{f}_I^{b^2} \quad \mathbf{f}_I^{b^3} \quad \mathbf{f}_I^{b^4}\}. \tag{35}$$

The submatrices and vectors in Equations (34) and (35) are:

$$\mathbf{K}_{IJ}^{rs} = \int_{\Omega^e} (\mathbf{B}_I^r)^T \mathbf{C} \mathbf{B}_J^s \mathrm{d}\Omega \qquad (r, s = u, a, b), \tag{36a}$$

$$\mathbf{f}_I^u = \int_{\partial\Omega_t^h \cap \partial\Omega^e} \hat{N}_I \bar{\mathbf{t}} \mathrm{d}\Gamma, \tag{36b}$$

$$\mathbf{f}_I^a = \int_{\partial\Omega_t^h \cap \partial\Omega^e} \hat{N}_I H \bar{\mathbf{t}} \mathrm{d}\Gamma, \tag{36c}$$

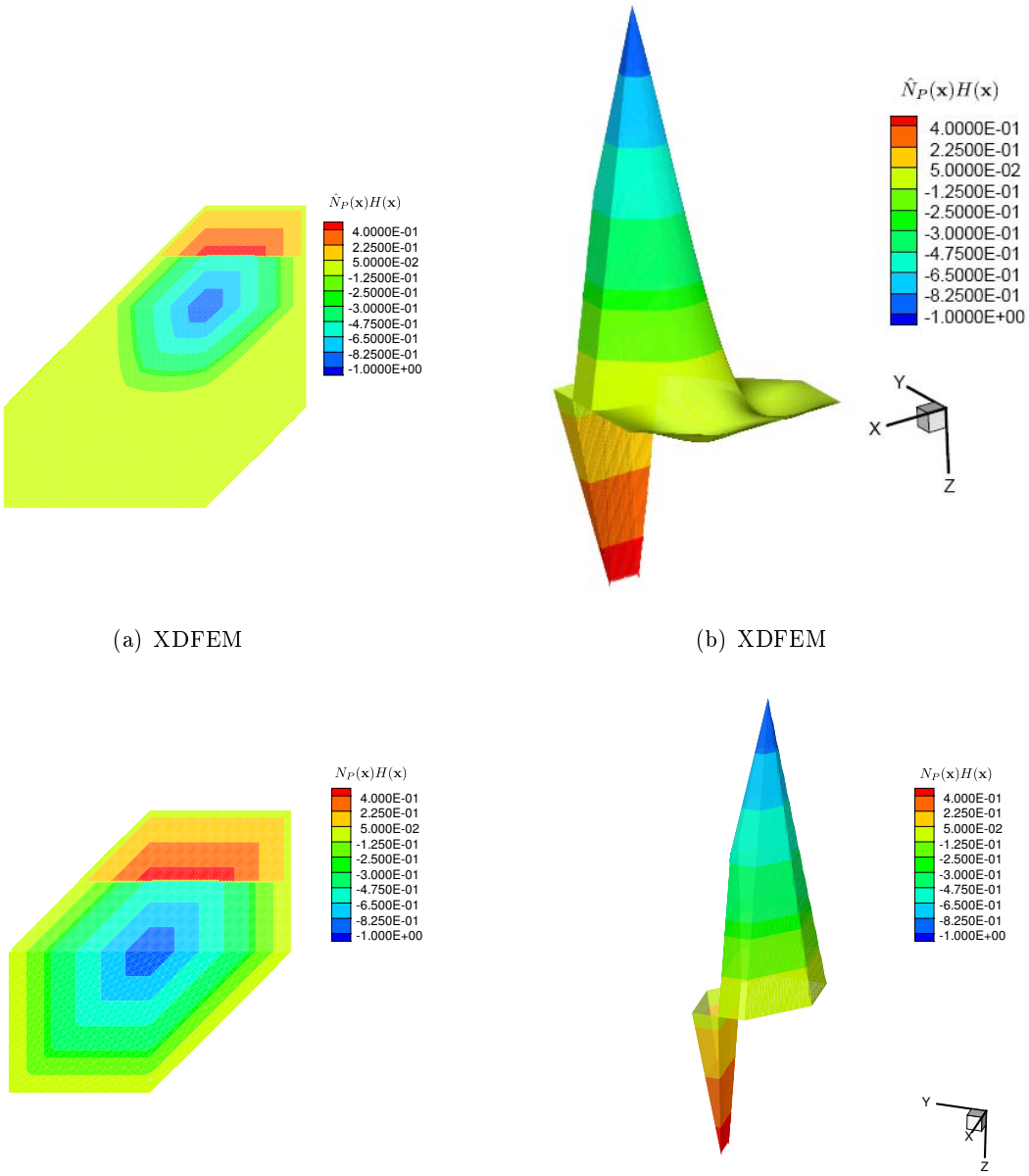

(a) XDFEM (b) XDFEM

(c) XFEM (d) XFEM

Figure 9: Contour plot of Heaviside enriched shape functions

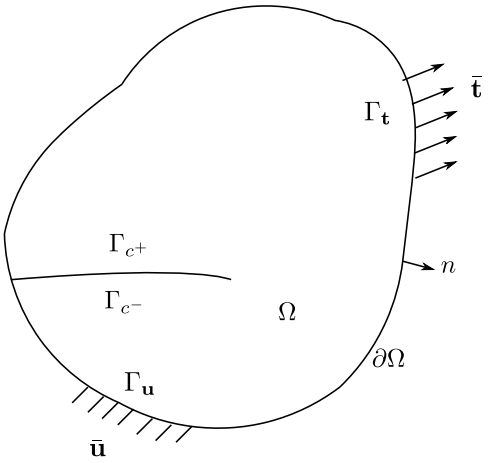

Figure 10: Elastic body with a crack

$$\mathbf{f}_I^{b^\alpha} = \int_{\partial\Omega_t^h \cap \partial\Omega^e} \hat{N}_I f_\alpha \bar{\mathbf{t}} \mathrm{d}\Gamma \qquad (\alpha = 1, 2, 3, 4). \tag{36d}$$

In Equation (36a), $\mathbf{B}_I^u, \mathbf{B}_I^q$ and $\mathbf{B}_I^{b^\alpha}$ are given by

$$\mathbf{B}_I^u = \begin{bmatrix} \hat{N}_{I,x} & 0 \\ 0 & \hat{N}_{I,y} \\ \hat{N}_{I,y} & \hat{N}_{I,x} \end{bmatrix}, \tag{37a}$$

$$\mathbf{B}_I^q = \begin{bmatrix} \left(\hat{N}_I(H - H_I)\right)_{,x} & 0 \\ 0 & \left(\hat{N}_I(H - H_I)\right)_{,y} \\ \left(\hat{N}_I(H - H_I)\right)_{,y} & \left(\hat{N}_I(H - H_I)_{,x}\right) \end{bmatrix}, \tag{37b}$$

$$\mathbf{B}_I^b = \begin{bmatrix} \mathbf{B}_I^{b^1} & \mathbf{B}_I^{b^2} & \mathbf{B}_I^{b^3} & \mathbf{B}_I^{b^4} \end{bmatrix}, \tag{37c}$$

$$\mathbf{B}_I^{b^\alpha} = \begin{bmatrix} \left(\hat{N}_I(f_\alpha - f_{\alpha I})\right)_{,x} & 0 \\ 0 & \left(\hat{N}_I(f_\alpha - f_{\alpha I})\right)_{,y} \\ \left(\hat{N}_I(f_\alpha - f_{\alpha I})\right)_{,y} & \left(\hat{N}_I(f_\alpha - f_{\alpha I})\right)_{,x} \end{bmatrix} \quad (\alpha = 1 - 4). \tag{37d}$$

In order to obtain the nodal displacements in a more straightforward manner, the shifted-basis is adopted in the above equations. More details regarding XFEM implementation can be referred in [12].

4 Numerical examples

A set of numerical examples is chosen to assess the efficiency and usefulness of the double-interpolation and its enriched form. In order to assess the convergence rate of each method, the relative error measured in the displacement L_2 norm and the energy norm are defined, respectively, as:

$$R_d = \sqrt{\frac{\int_\Omega (\mathbf{u}^h - \mathbf{u})^{\mathrm{T}} (\mathbf{u}^h - \mathbf{u}) \mathrm{d}\Omega}{\int_\Omega \mathbf{u}^{\mathrm{T}} \mathbf{u} \mathrm{d}\Omega}}, \tag{38a}$$

$$R_e = \sqrt{\frac{\int_\Omega (\boldsymbol{\sigma}^h - \boldsymbol{\sigma})^{\mathrm{T}} (\boldsymbol{\epsilon}^h - \boldsymbol{\epsilon}) \mathrm{d}\Omega}{\int_\Omega \boldsymbol{\sigma}^{\mathrm{T}} \boldsymbol{\epsilon} \mathrm{d}\Omega}}. \tag{38b}$$

where, the fields with superscript 'h' refer to the approximation, and $\boldsymbol{\sigma}, \boldsymbol{\epsilon}, \mathbf{u}$ are exact fields. Unless specified otherwise, the *Young's modulus* E and *Possion's ratio* ν are assumed to be 1000 and 0.3 respectively. The constants μ and κ are given by:

$$\mu = \frac{E}{2(1+\nu)}, \tag{39a}$$

$$\kappa = \begin{cases} 3 - 4\nu, & \text{Plane strain} \\ (1-\nu)/(3+\nu), & \text{Plane stress} \end{cases}$$

4.1 Higher-order convergence test

The first example will investigate the precision and convergence rate of DFEM in comparison with the 3-noded triangular element (T3) and 6-noded triangular element (T6) by solving the Laplace equation:

$$-\Delta u = f, \quad \text{on } \Omega, \tag{40a}$$

$$u = \bar{u} = 0, \quad \text{on } \partial\Omega. \tag{40b}$$

where Δ is the Laplace operator, u the scalar primary variable and f the source term. Here the domain Ω is selected as a square area with a dimension $[-1,1] \times [-1,1] \subset \mathbb{R}^2$. And f is given as:

$$f = 5\pi^2 \mathrm{sin}(2\pi x)\mathrm{sin}(\pi y). \tag{41}$$

And the analytical solution of u and its derivatives $u_{,x}$, $u_{,y}$ can be found as:

$$u = \mathrm{sin}(2\pi x)\mathrm{sin}(\pi y), \tag{42a}$$

$$u_{,x} = 2\pi \mathrm{cos}(2\pi x)\mathrm{sin}(\pi y), \tag{42b}$$

$$u_{,y} = \pi \mathrm{sin}(2\pi x)\mathrm{cos}(\pi y). \tag{42c}$$

And errors of the L_2 and energy norm of the primary variable are defined as:

$$R_d = \sqrt{\frac{\int_\Omega (u^h - u)^2 \mathrm{d}\Omega}{\int_\Omega u^2 \mathrm{d}\Omega}}, \tag{43a}$$

$$R_e = \sqrt{\frac{\int_\Omega (\nabla u^h - \nabla u)^{\mathrm{T}} (\nabla u^h - \nabla u) \mathrm{d}\Omega}{\int_\Omega (\nabla u)^{\mathrm{T}} \nabla u \mathrm{d}\Omega}}. \tag{43b}$$

Figure 11 shows all the convergence curves with respective to the element size of each element. We use m to denote the slope of the convergence curve. From this figure we note that DFEM achieves a convergence rate in the displacement norm ($2 < m = 2.63 < 3$) and the energy norm ($1 < m = 1.69 < 2$), both of which are between the linear and quadratic Lagrange finite elements. And the precision of DFEM is improved by $O(10^{-1})$ than FEM(T3) noting that their total DOFs is the same.

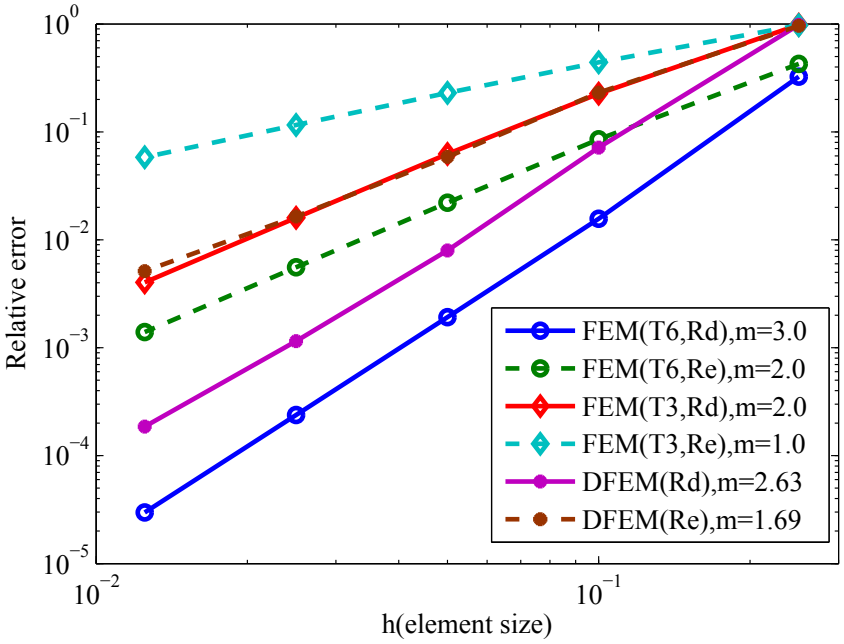

Figure 11: results of the higher-order convergence test

4.2 Infinite plate with a hole

Figure 12 presents the upper right quadrant of an infinite plate with a center hole subjected to remote tensile loads. The geometrical parameters are $L = 5$ and $a = 1$. The analytical solutions for stress and displacement fields are given as [49]:

$$\sigma_{xx}(r,\theta) = 1 - \frac{a^2}{r^2}\left(\frac{3}{2}\cos 2\theta + \cos 4\theta\right) + \frac{3a^4}{2r^4}\cos 4\theta, \tag{44a}$$

$$\sigma_{yy}(r,\theta) = -\frac{a^2}{r^2}\left(\frac{1}{2}\cos 2\theta - \cos 4\theta\right) - \frac{3a^4}{2r^4}\cos 4\theta, \tag{44b}$$

$$\tau_{xy}(r,\theta) = 1 - \frac{a^2}{r^2}\left(\frac{1}{2}\sin 2\theta + \sin 4\theta\right) + \frac{3a^4}{2r^4}\sin 4\theta, \tag{44c}$$

$$u_r(r,\theta) = \frac{a}{8\mu}\left[\frac{r}{a}(\kappa+1)\cos\theta + \frac{2a}{r}((1+\kappa)\cos\theta + \cos 3\theta) - \frac{2a^3}{r^3}\cos 3\theta\right], \tag{44d}$$

$$u_\theta(r,\theta) = \frac{a}{8\mu}\left[\frac{r}{a}(\kappa-1)\sin\theta + \frac{2a}{r}((1-\kappa)\sin\theta + \sin 3\theta) - \frac{2a^3}{r^3}\sin 3\theta\right], \tag{44e}$$

where (r,θ) are the polar coordinates. The exact traction is imposed on the top and right boundary of the model. The number of nodes used in the four models are 121, 441, 1681 and 6561.

In this example, the numerical results obtained using DFEM, FEM(T3) and FEM(T6) are compared for the same mesh discretization. The relative error in the displacement and energy norm for this example are plotted in Figures 13 and 14, respectively. It can be observed DFEM exceeds the linear optimal convergence rate slightly in the displcement norm, but the error shows an level close to one order of magnitude less than that of T3 elements. In the energy norm, the DFEM converges 34% faster than the T3 but 31% slower than the T6, thus providing an intermediate behavior between the two triangular elements.

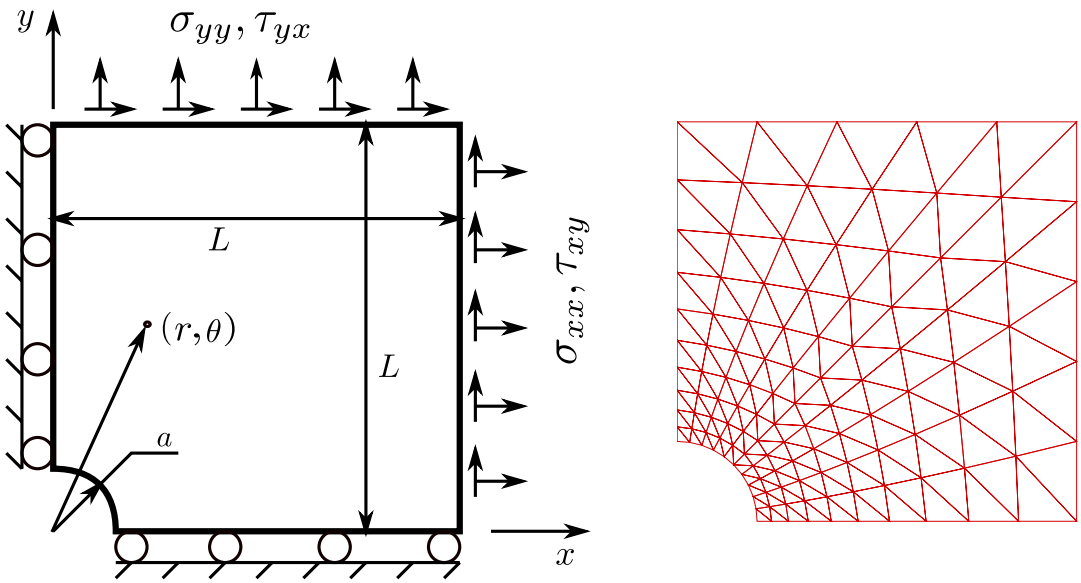

Figure 12: (a) 1/4 model of the infinite plate with a center hole; (b) The typical mesh division

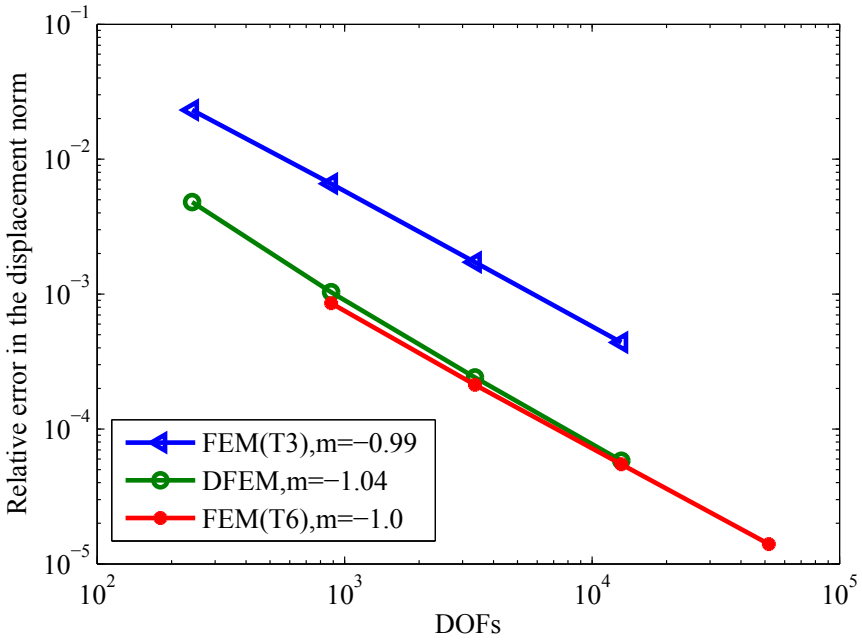

Figure 13: Relative error in the displacement norm for an infinite plate with a hole

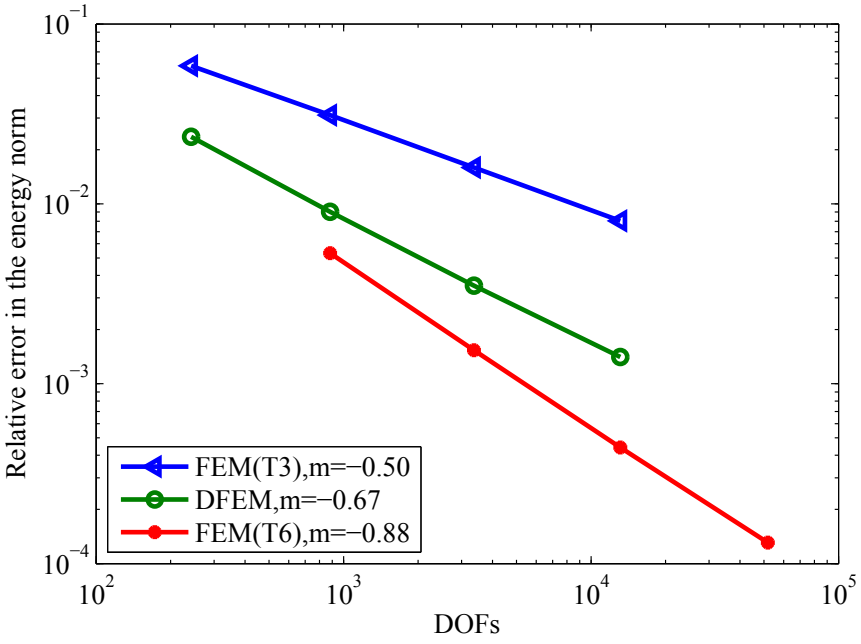

Figure 14: Relative error in the energy norm for an infinite plate with a hole

4.3 Timoshenko Beam

Figure 15 illustrates a continuum model of a cantilever beam. In this example, plane stress conditions are assumed. The geometric parameters are taken as $L = 48$ and $W = 12$. The analytical displacement and stress fields are given in [49] as:

$$u_x(x,y) = \frac{Py}{6EI}\left[(6L-3x)x + (2+\nu)(y^2 - \frac{W^2}{4})\right], \tag{45a}$$

$$u_y(x,y) = -\frac{P}{6EI}\left[3\nu y^2(L-x) + (4+5\nu)\frac{W^2 x}{4} + (3L-x)x^2\right], \tag{45b}$$

$$\sigma_{xx}(x,y) = \frac{P(L-x)y}{I}, \tag{45c}$$

$$\sigma_{yy}(x,y) = 0, \tag{45d}$$

$$\tau_{xy}(x,y) = -\frac{P}{2I}\left(\frac{W^2}{4} - y^2\right). \tag{45e}$$

where $P = 1000.$ and $I = W^3/12$. The exact displacement is applied to the left boundary and the exact traction is applied to the right boundary.

Structured meshes are used in this example to ensure regular node location and to enable easier comparison among the T3, T6, Q4 and DFEM (Figure 16). Four mesh sizes, 3×10, 6×20, 12×40 and 24×80, are used. It can be observed that, the DFEM solution demonstrates better accuracy and is super-convergent in the displacement and energy norm by more than 50% compared to Q4 and T3, but less than T6 in both accuracy and convergence rate.

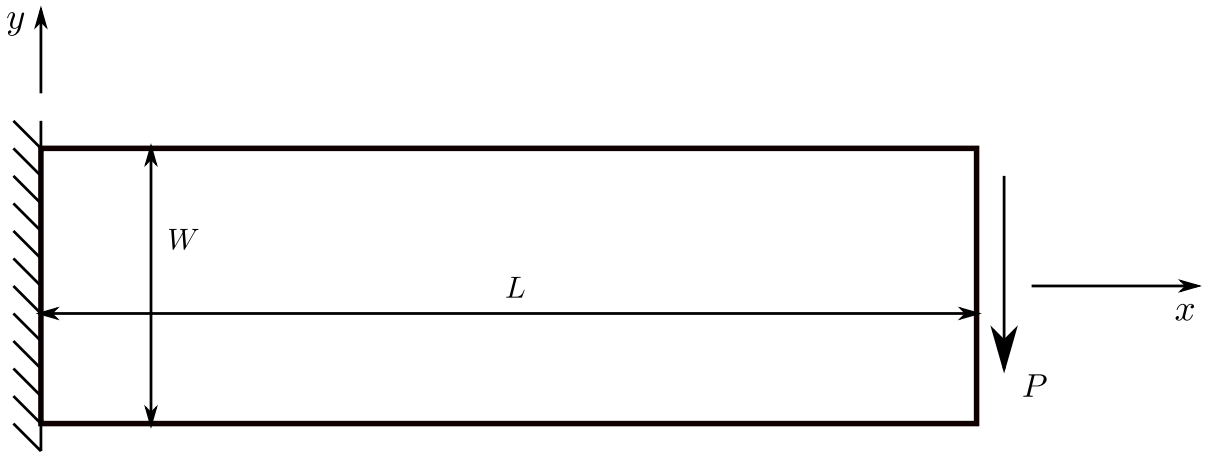

Figure 15: Physical model of cantilever beam

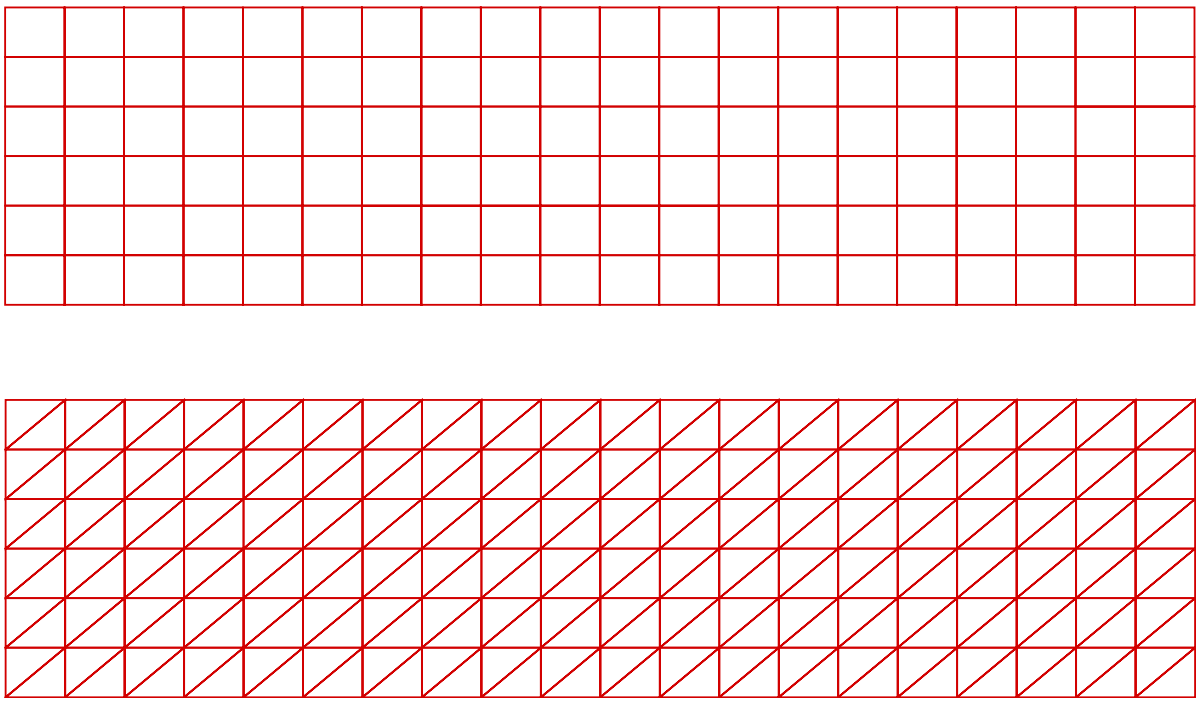

Figure 16: Mesh discretization using regular quadrilateral and triangular elements

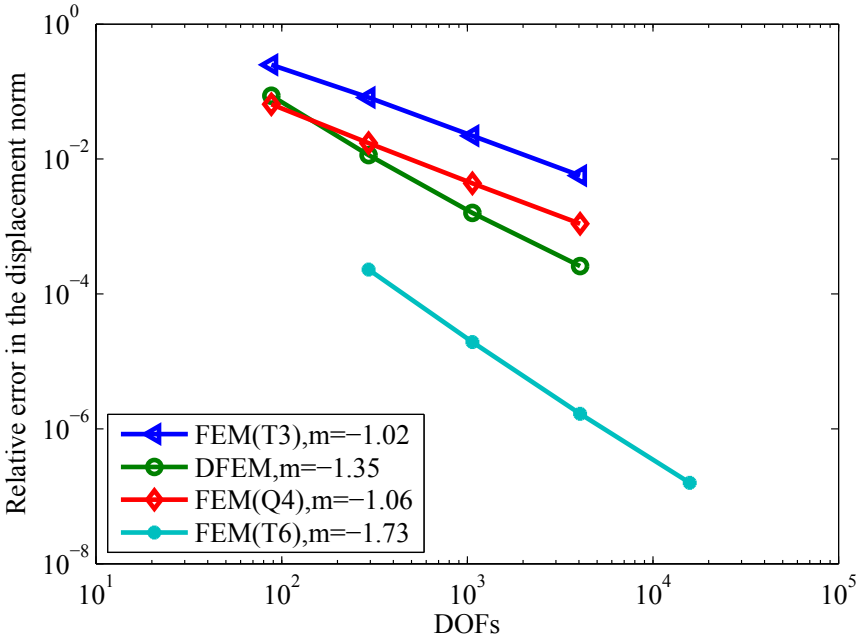

(a)

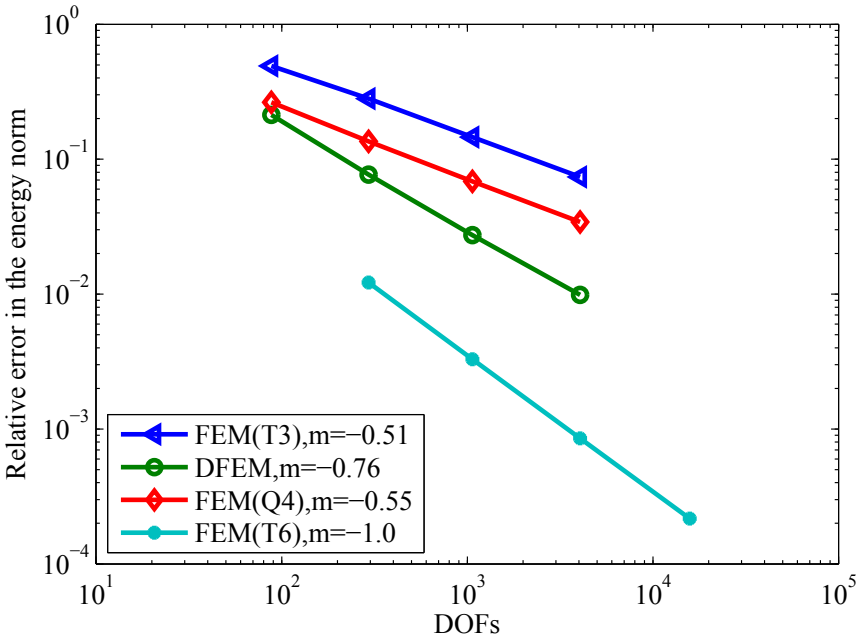

(b)

Figure 17: Relative error in displacement and energy norm of Timoshenko beam

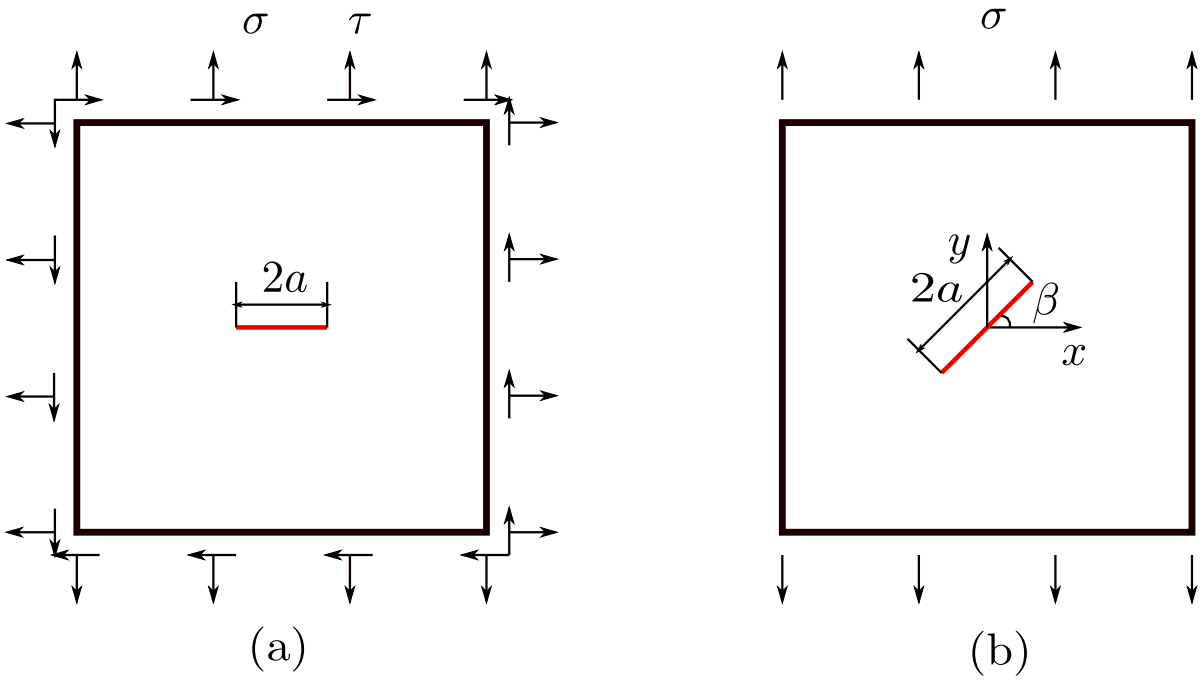

Figure 18: (a)Griffith crack; (b) inclined crack

4.4 Griffith crack

A Griffith crack problem is shown in Figure 18(a). An infinite plate with a crack segment (a=1.) subjected to remote tensile loads is considered here. A square domain (10×10) is selected in the vicinity of the crack tip. The analytical displacement and stress fields are given by [50]:

$$\begin{aligned}\sigma_{xx}(r,\theta) =& \frac{K_I}{\sqrt{2\pi r}}\cos\frac{\theta}{2}\left(1-\sin\frac{\theta}{2}\sin\frac{3\theta}{2}\right)\\ &-\frac{K_{II}}{\sqrt{2\pi r}}\sin\frac{\theta}{2}\left(2+\cos\frac{\theta}{2}\cos\frac{3\theta}{2}\right),\end{aligned} \tag{46a}$$

$$\sigma_{yy}(r,\theta) = \frac{K_I}{\sqrt{2\pi r}}\cos\frac{\theta}{2}\left(1+\sin\frac{\theta}{2}\sin\frac{3\theta}{2}\right)+\frac{K_{II}}{\sqrt{2\pi r}}\sin\frac{\theta}{2}\cos\frac{\theta}{2}\cos\frac{3\theta}{2}, \tag{46b}$$

$$\tau_{xy}(r,\theta) = \frac{K_I}{\sqrt{2\pi r}}\sin\frac{\theta}{2}\cos\frac{\theta}{2}\cos\frac{3\theta}{2}+\frac{K_{II}}{\sqrt{2\pi r}}\cos\frac{\theta}{2}\left(1-\sin\frac{\theta}{2}\sin\frac{3\theta}{2}\right), \tag{46c}$$

$$\begin{aligned}u_x(r,\theta) =& \frac{K_I}{2\mu}\sqrt{\frac{r}{2\pi}}\cos\frac{\theta}{2}\left(\kappa-1+2\sin^2\frac{\theta}{2}\right)\\ &+\frac{(1+\nu)K_{II}}{E}\sqrt{\frac{r}{2\pi}}\sin\frac{\theta}{2}\left(\kappa+1+2\cos^2\frac{\theta}{2}\right),\end{aligned} \tag{46d}$$

$$\begin{aligned}u_y(r,\theta) =& \frac{K_I}{2\mu}\sqrt{\frac{r}{2\pi}}\sin\frac{\theta}{2}\left(\kappa+1-2\cos^2\frac{\theta}{2}\right)\\ &+\frac{(1+\nu)K_{II}}{E}\sqrt{\frac{r}{2\pi}}\cos\frac{\theta}{2}\left(1-\kappa+2\sin^2\frac{\theta}{2}\right),\end{aligned} \tag{46e}$$

where K_I and K_{II} are the stress intensity factors (SIFs) for mode-I and mode-II, respectively. (r,θ) are the polar coordinates used to define the crack geometry.

4.4.1 Convergence study

The Griffith crack problem is first used to investigate the enrichment effects of DFEM. The convergence rate in XDFEM is studied in three folds: explicit crack representation (where the crack is explicitly meshed), Heaviside enrichment only and full Heaviside and asymptotic enrichment. These results are plotted in Figure 19. From Figure 19, it can be concluded that the DFEM yields better accuracy and slightly improves the convergence rate compared to FEM for all the cases considered. It also transpires from the results that the full enrichment of DFEM produces better accuracy than modelling the crack explicitly.

1 million DOFs problems in both mode-I and mode-II were simulated to assess the convergence rate of the method(see Figures 20 and 21). The relative errors in the SIFs are also shown in the plots. We study the case where only tip enrichment is used, which is known [24][25] to lead to the same convergence rate as the standard Lagrange-based FEM, and which is confirmed here also for XDFEM as expected. We also observe that XDFEM is, as XFEM, able to reproduce the discontinuity across the crack faces. When geometrical enrichment with an enrichment radius to be 1/5 of the crack length is used (Figure 22), optimality is recovered and the XDFEM solution is also more accurate than the XFEM solution in terms of displacement, energy and SIFs. Figure 23 illustrates the number of iteration required for the Conjugate Gradient (CG) solver to converge, which can be regarded as an indication to the condition number of the stiffness matrix. It is observed that XDFEM performs slightly worse than XFEM in terms of the condition number. And the deterioration rate of fixed area enrichment is much higher than standard enrichment in both methods. These conclusions are in agreement with the investigation reported in [24][26].

4.4.2 Accuracy study

Though it has been already established from the convergence curves that over the whole computational domain, the XDFEM is generally slightly more accurate than XFEM for a given number of DOFs, it is necessary to investigate whether XDFEM improves the precision also locally in the vicinity of the crack tip. The strain component ϵ_{yy} is plotted along the line perpendicular to the crack in front of the tip (the line $x = 0$) in a 31×31 structured mesh in Figure 24. It can be noted from Figure 24, that the XDFEM result is much closer to the analytical solution than that of XFEM. Especially, in the vicinity of the crack tip, the XDFEM performs better due to the inclusion of nodal gradients in the approximation.

The mesh distortion effect is also investigated in this example. The strutured mesh and typical distorted mesh are shown in Figure 25. The results are listed in Table 1. And the precision of XDFEM in distorted mesh appears to be superior than that of the XFEM.

	Strutured mesh		distorted mesh	
DOFs	XFEM	XDFEM	XFEM	XDFEM
334	0.2272	0.1832	0.2313	0.1882
4726	0.1112	0.08672	0.1132	0.08863
7834	0.09769	0.07600	0.1016	0.08261
17134	0.08006	0.06212	0.08223	0.06215

Table 1: Relative error in the energy norm for regular structured meshes and distorted meshes

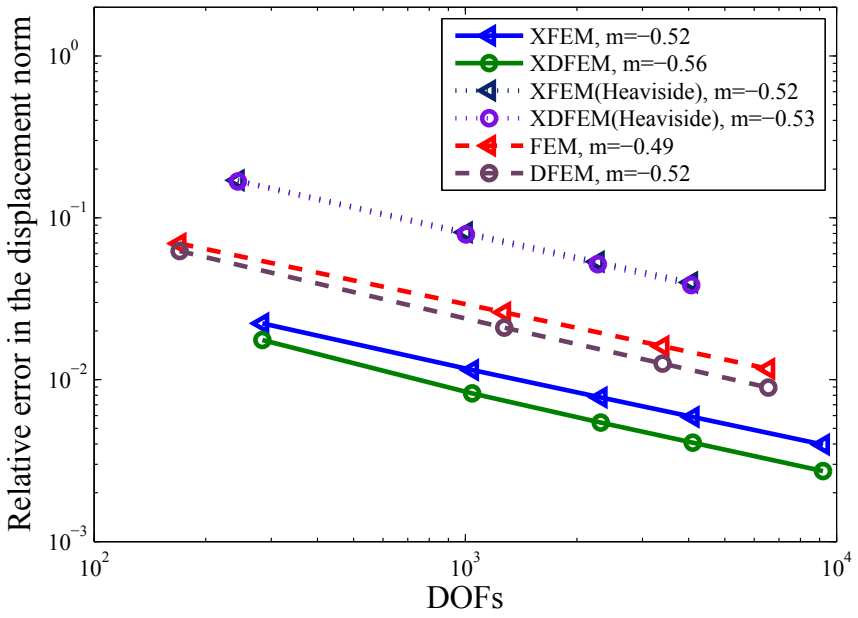

(a)

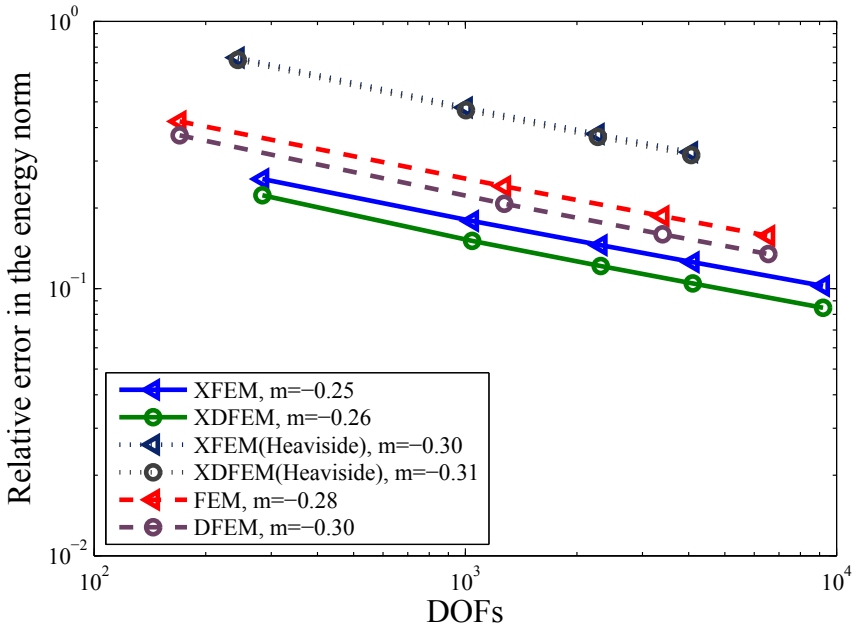

(b)

Figure 19: Relative error in the displacement and energy norm of in Griffith crack for explicit crack representation(dashed lines), Heaviside enrichment only (dotted lines) and topological enrichment (solid lines)

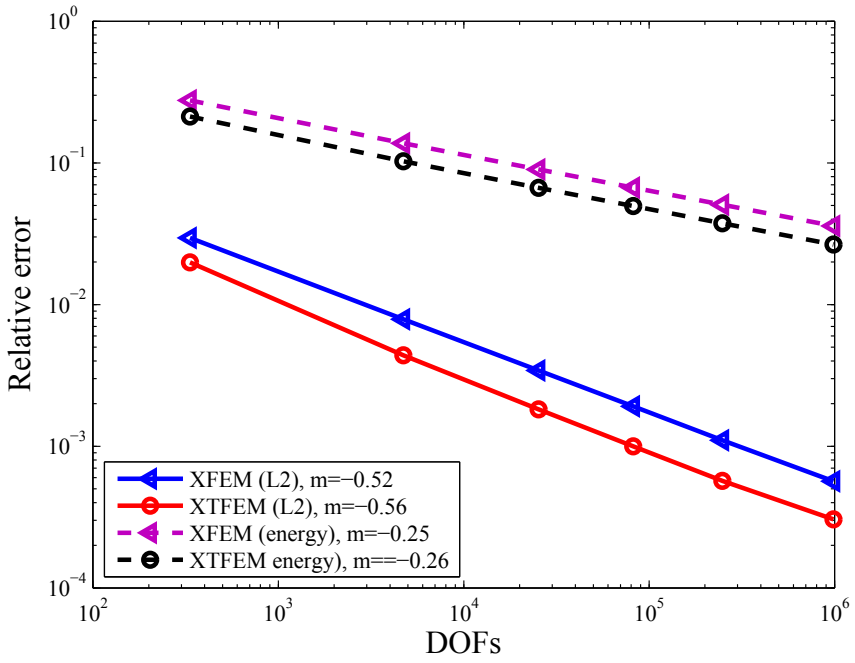

(a)

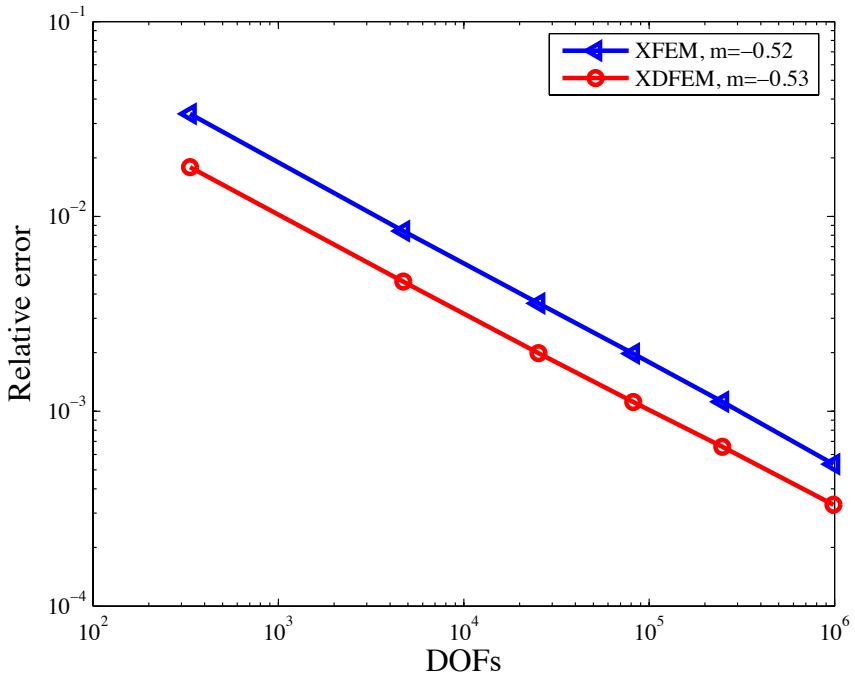

(b)

Figure 20: Convergence results of Griffith crack (mode-I) for topological enrichment: (a) the error in the displacement L_2 and energy norm; (b) the error in SIFs

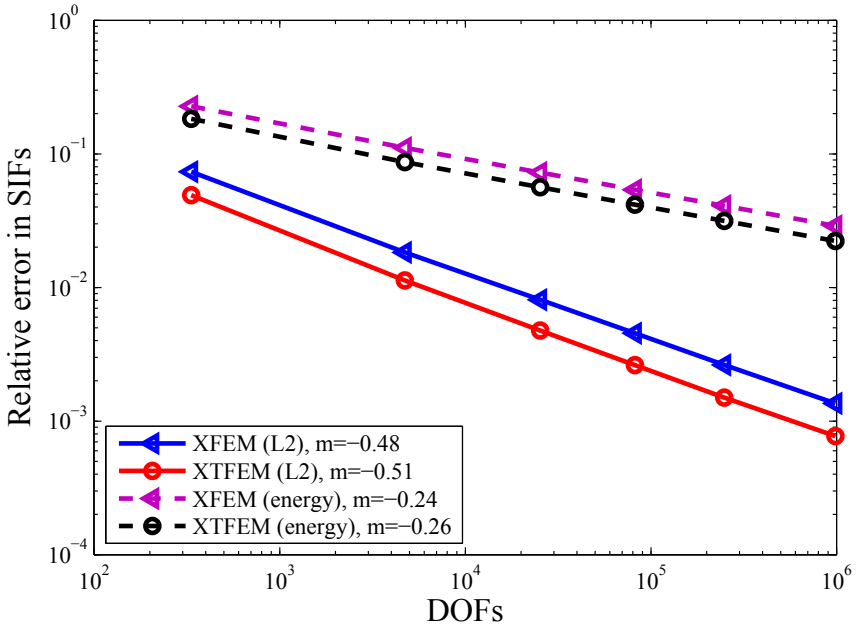

(a)

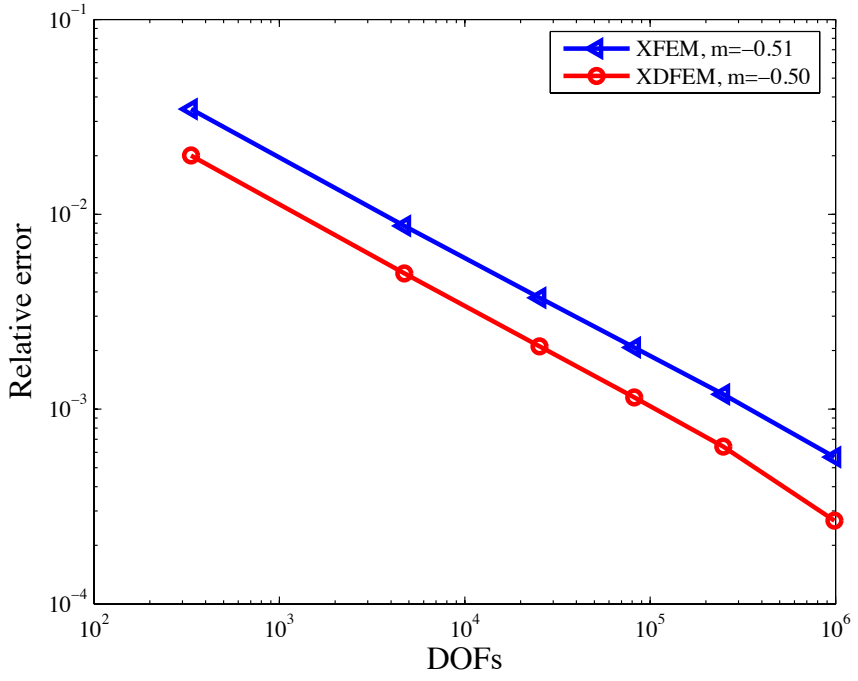

(b)

Figure 21: Convergence results of Griffith crack (mode-II) for topological enrichment: (a) the error in the displacement L_2 and energy norm; (b) the error in SIFs

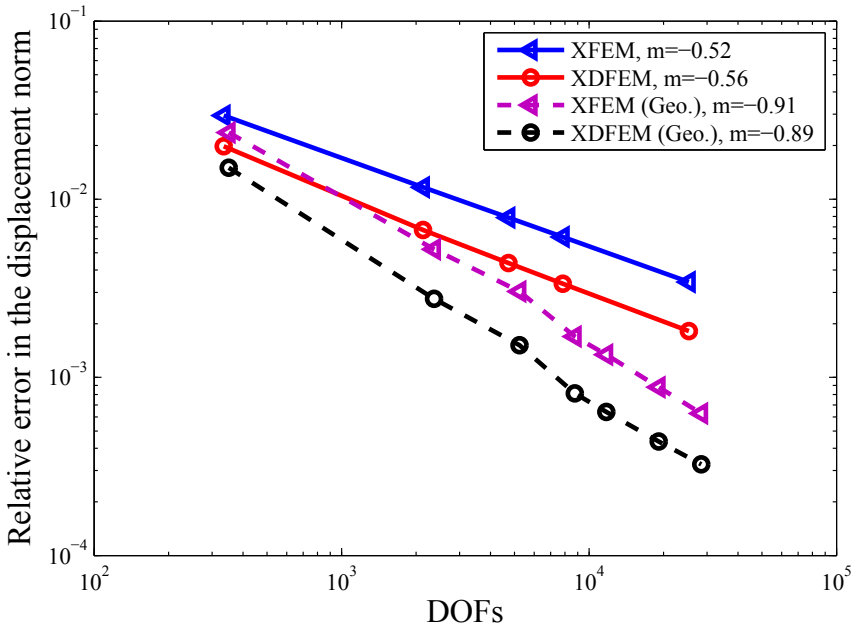

(a)

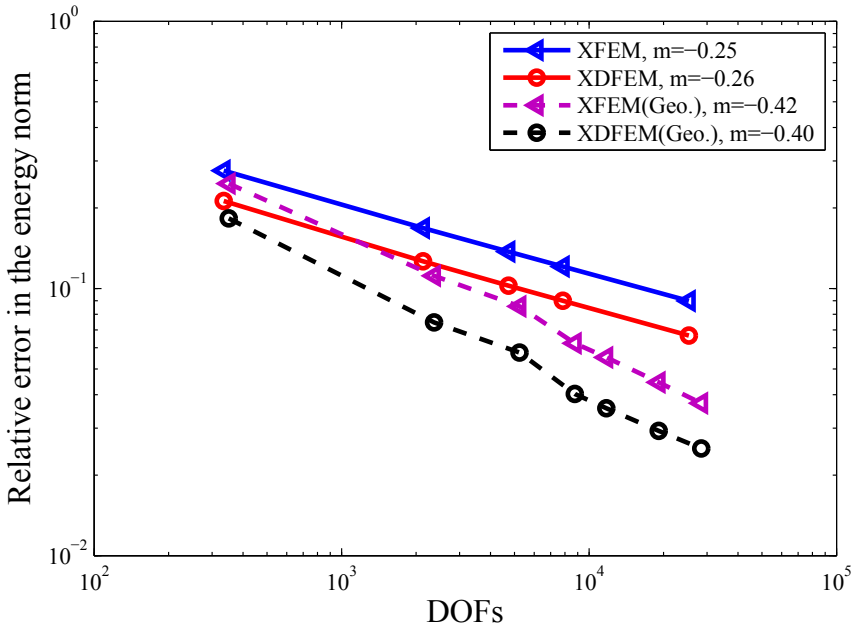

(b)

Figure 22: Convergence results of topological enrichment (solid lines) and geometrical enrichment (Geo., dashed lines) for mode-I: (a) the error in the displacement L_2 norm; (b) the error in the energy norm

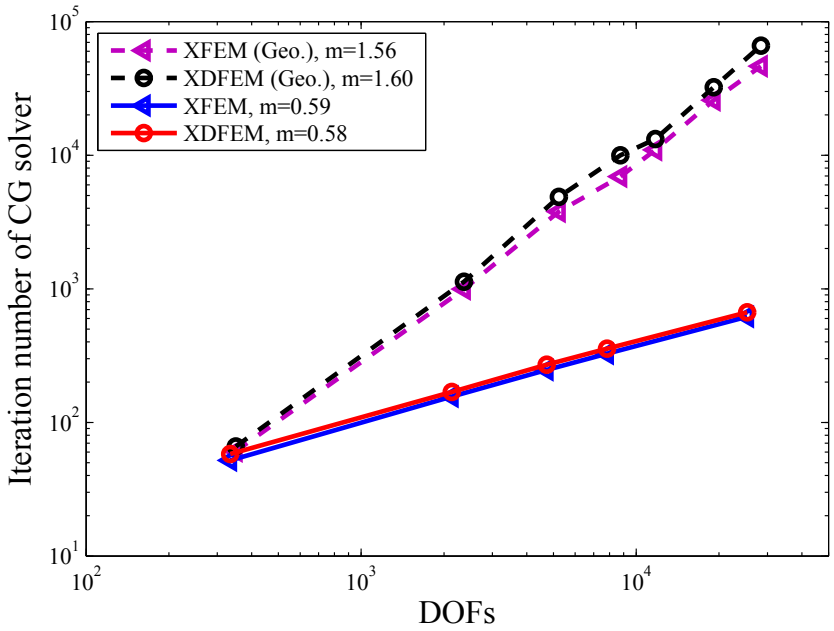

Figure 23: Iteration number of CG solver; solid lines for topological enrichment, dashed lines for geometrical enrichment

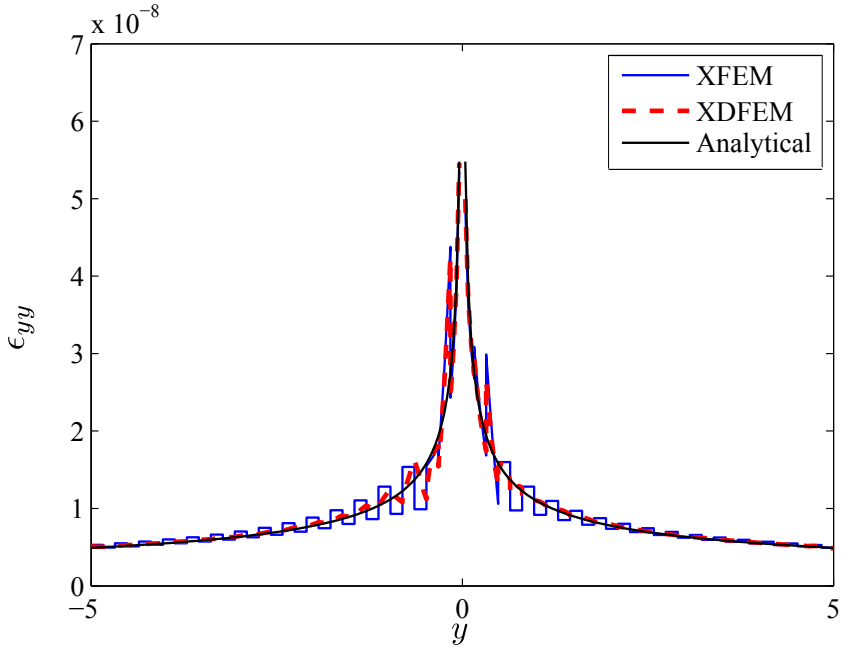

Figure 24: The comparison of the strain component along line $x = 0$

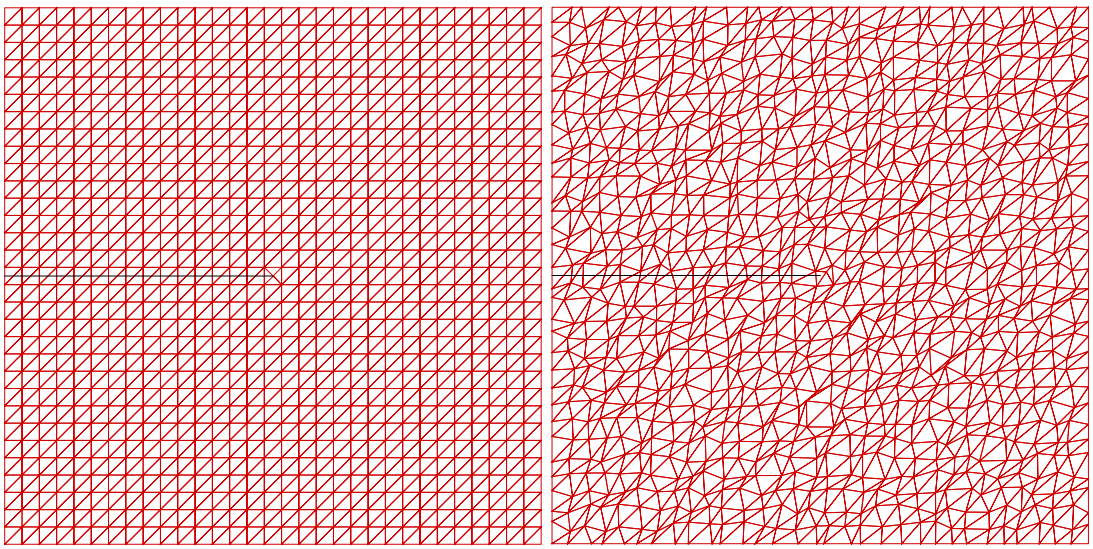

(a) (b)

Figure 25: Mesh design to check the mesh distortion effect:(a)structured mesh;(b) distorted mesh

4.4.3 Computational efficiency

It should be highlighted that the support domain of DFEM element is much bigger than that of FEM element due to the introduction of the nodal gradient into the approximation (see Figure 1, Figure 5). This directly results in increased bandwidth of the stiffness matrix in DFEM. Consequently, the computational time per DOFs is expected to be larger for DFEM than for the FEM. Figure 26 and 27(a) show the comparison of the time cost in assembling the stiffness matrix, solving the linear equations and the total time of the two processes. It can be seen that with the model size increasing, XDFEM requires less time to obtain the same precision. For the solution process, XFEM produces an error 1.4 times higher ($\frac{XFEM15.48}{XDFEM11.} = 1.4$) than the XDFEM at the same computational time of 0.06 seconds. The total time comparison shows that after $t_0 = 0.6$ seconds, XDFEM is more efficient computationally than XFEM in terms of the energy error. It can be observed from Figure 27(b) that XDFEM is always superior to XFEM in the same DOFs. The main cause of the increased cost associated with XDFEM is the increased bandwidth. This can be alleviated by using an 'element-by-element' approach.

4.5 Inclined center crack

An inclined crack problem is investigated in this section. The model is presented in Figure 18(b). The infinite plate is subjected to remote tensile load in y direction and the inclination angle β is measured in the counter-clockwised direction from the x direction. The half crack length is $a = 1$. A square domain field (10×10) encircling the crack tip is selected and the exact displacement is applied on the boundary, as in the previous example. The analytical SIFs are given as

$$K_I = \sigma\sqrt{\pi a}\cos^2\beta, \tag{47a}$$

$$K_{II} = \sigma\sqrt{\pi a}\cos\beta\sin\beta. \tag{47b}$$

Table 2 shows the relative error of K_I and K_{II} varying with the inclination angle of the crack. It can be observed from Table 2 that both XDFEM and XFEM results agree well with the analytical solution. The precision of the SIFs in the XDFEM are better than that of the

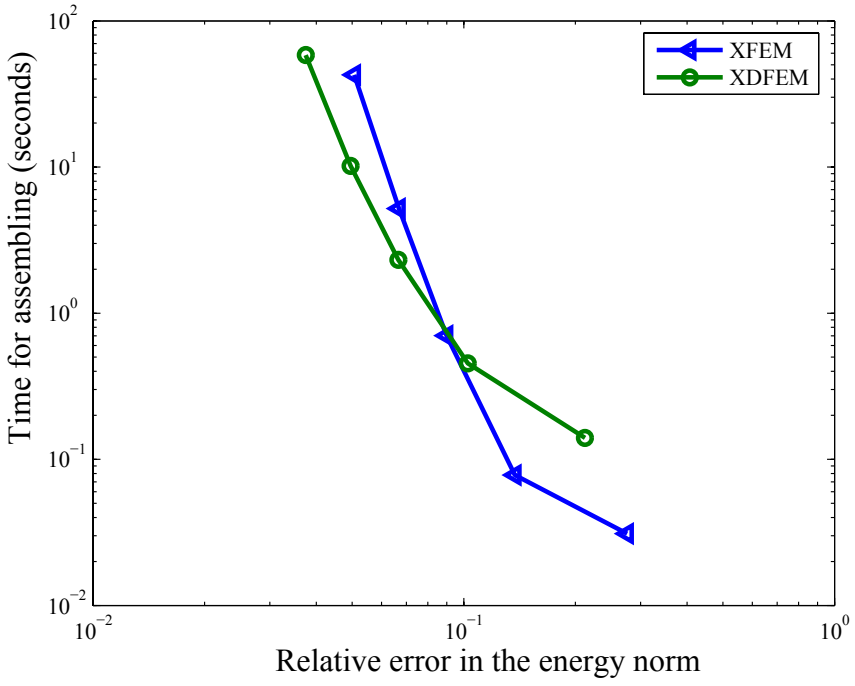

(a)

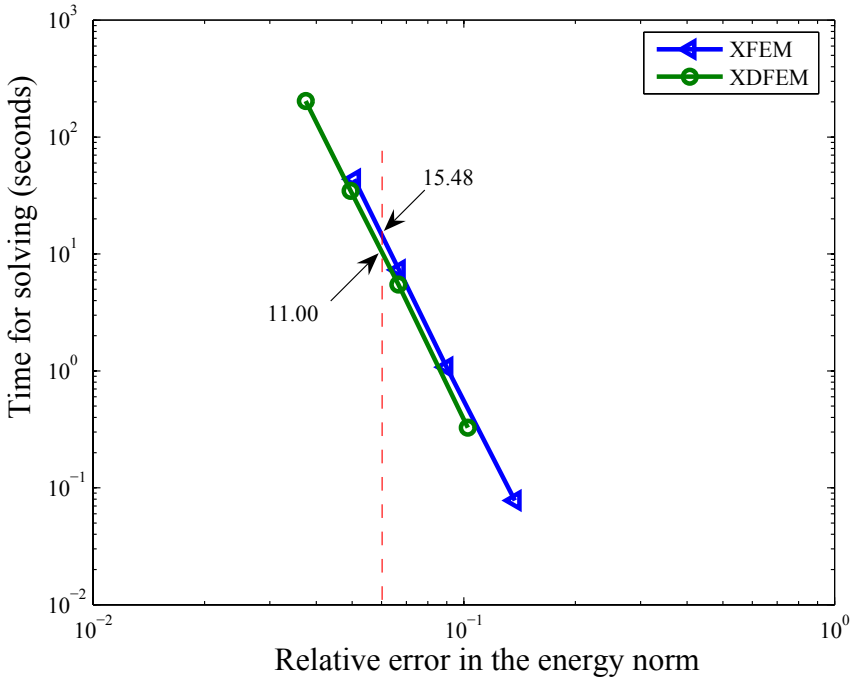

(b)

Figure 26: Comparison of time costs for XFEM and XDFEM in Griffith crack problem

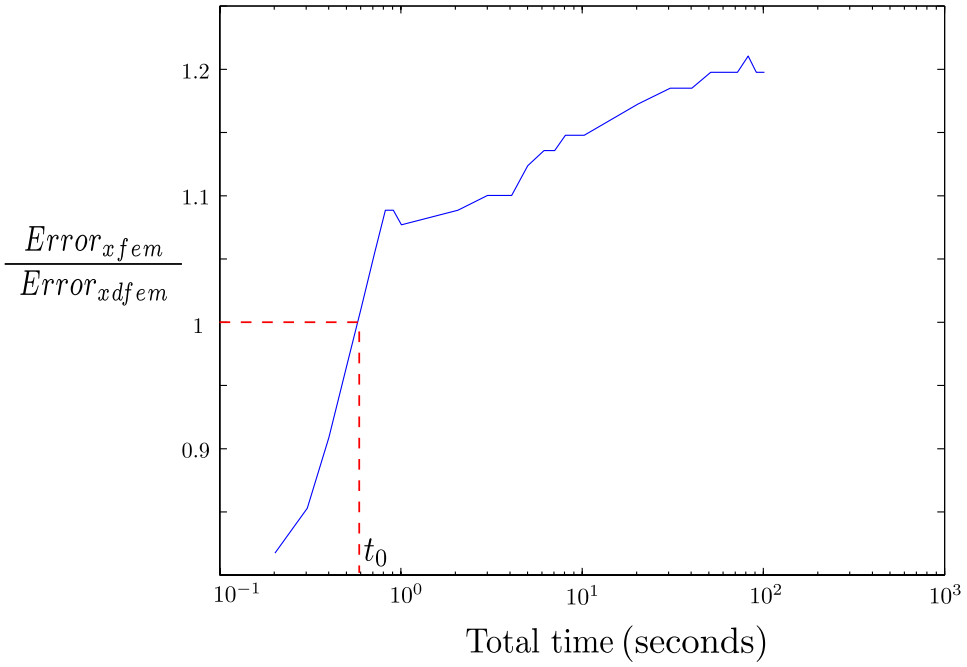

(a)

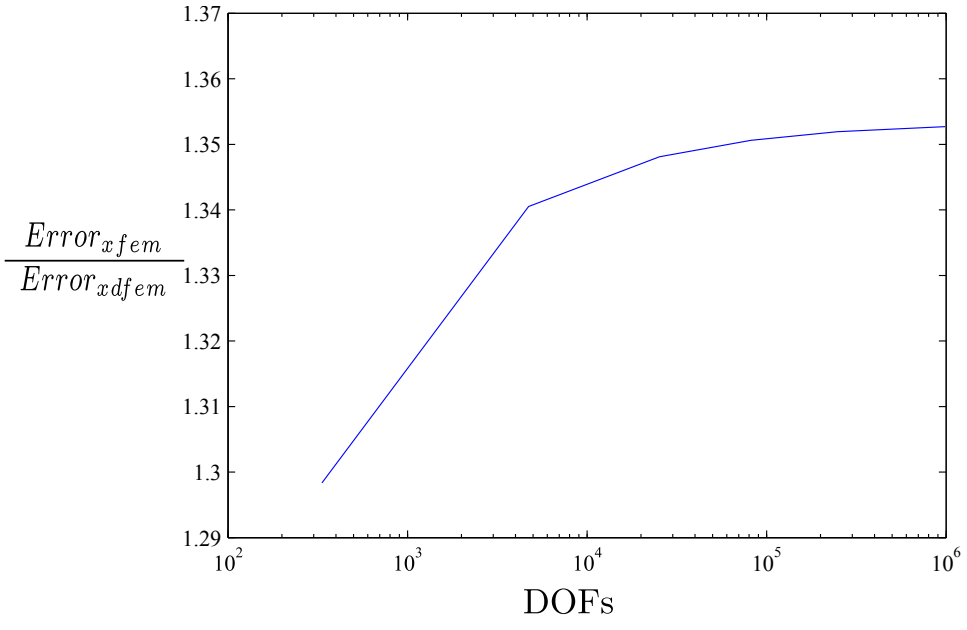

(b)

Figure 27: The comparison of the energy norm error in terms of (a) time; (b) DOFs

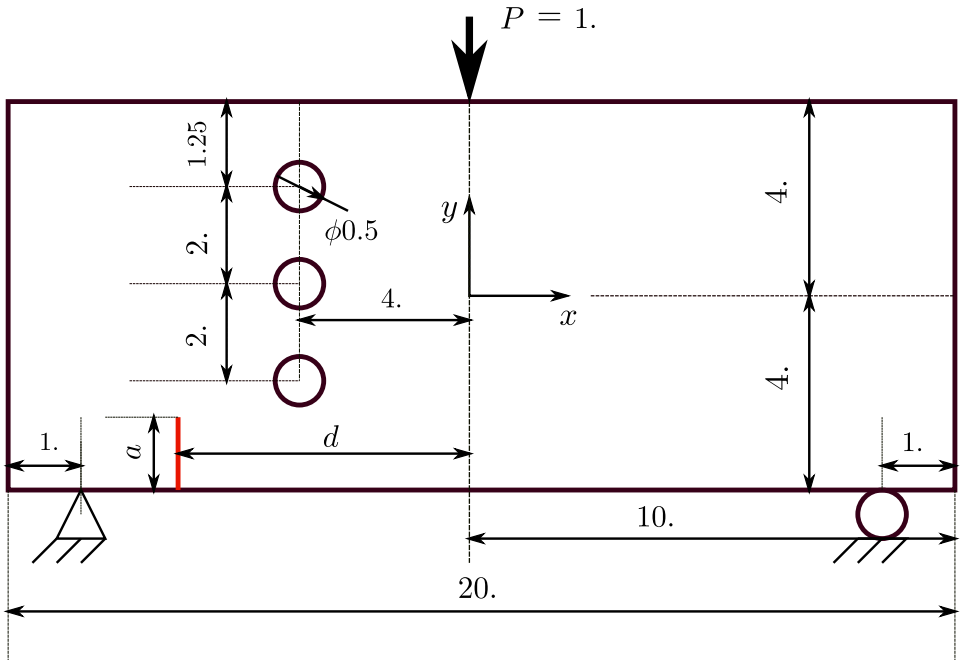

Figure 28: Physical model of three points bending beam with three holes

XFEM. This example demonstrates that XDFEM performs well also for the mixed mode crack problems.

	$K_I(\%)$		$K_{II}(\%)$	
β	XFEM	XDFEM	XFEM	XDFEM
0	0.58	0.29	0.03	0.10
$\frac{\pi}{12}$	0.54	0.28	0.07	0.12
$\frac{\pi}{6}$	0.49	0.26	0.30	0.20
$\frac{\pi}{4}$	0.43	0.23	0.36	0.21
$\frac{\pi}{3}$	0.32	0.20	0.41	0.23
$\frac{5\pi}{12}$	$< 10^{-3}$	0.14	0.43	0.23
$\frac{\pi}{2}$	$< 10^{-3}$	$< 10^{-3}$	$< 10^{-3}$	$< 10^{-3}$

Table 2: The error in the SIFs for the inclined center crack problem (47×47 structured mesh)

4.6 XDFEM for crack propagation

A three point bending beam with three holes is simulated in this section to test the versatility of XDFEM in simulating crack propagation. Holes strongly influence crack propagation in structures and the chosen example is a decisive test for computational fracture problems, as the crack path obtained is most sensitive to the accuracy of the crack driving force computation, as well as the chosen propagation increment, as will be seen below. This experiment is designed to explore the effect of holes on the crack trajectories. The geometry and load condition are illustrated in Figure 28. Plexiglas specimens are used for which $E = 1000$ and $\nu = 0.37$ is used in the simulations. Plane strain condition is assumed. With the variation of the position of the initial crack, different crack trajectories are obtained [51] [52]. A set of test cases, as listed in Table 3, are simulated. The maximum hoop stress criterion and the equivalent domain form of the interaction energy integral for SIFs extraction [1] is adopted to judge the orientation of

crack propagation. The model is discretized by 27869 nodes and 55604 triangular elements. Figure 29 illustrates the crack evolution of the listed three cases. And the results show that both methods are in good agreement with the experiment. In the numerical tests it is noted that, though, the error of energy norm decreases in XDFEM, the crack path is still very close to that of the XFEM. It can also be observed from Figure 29 that, there is very minor difference in the crack path trajectory between XFEM and XDFEM. However the crack paths obtained from both methods show a significant deviation when the crack passes through the hole in case 1 and case 3, which tends to make an influence to the final trajectories. We should somehow be aware that the different crack increment will affect the crack path as well declared in [53]. The SIFs for the three crack trajectories are plotted in Figure 30. It can be observed that the SIFs tend to change in a bigger amplitude when the crack goes through the hole in case 1 and case 3. The SIFs for each case compare well between the two methods. Figure 31 compares the stress contours of the XFEM and the XDFEM. The XDFEM provides smooth stress fields without any post-processing.

	d	a	crack increment	number of propagation
case 1	5	1.5	0.052	67
case 2	6	1.0	0.060	69
case 3	6	2.5	0.048	97

Table 3: Test cases for the three points bending beam problem

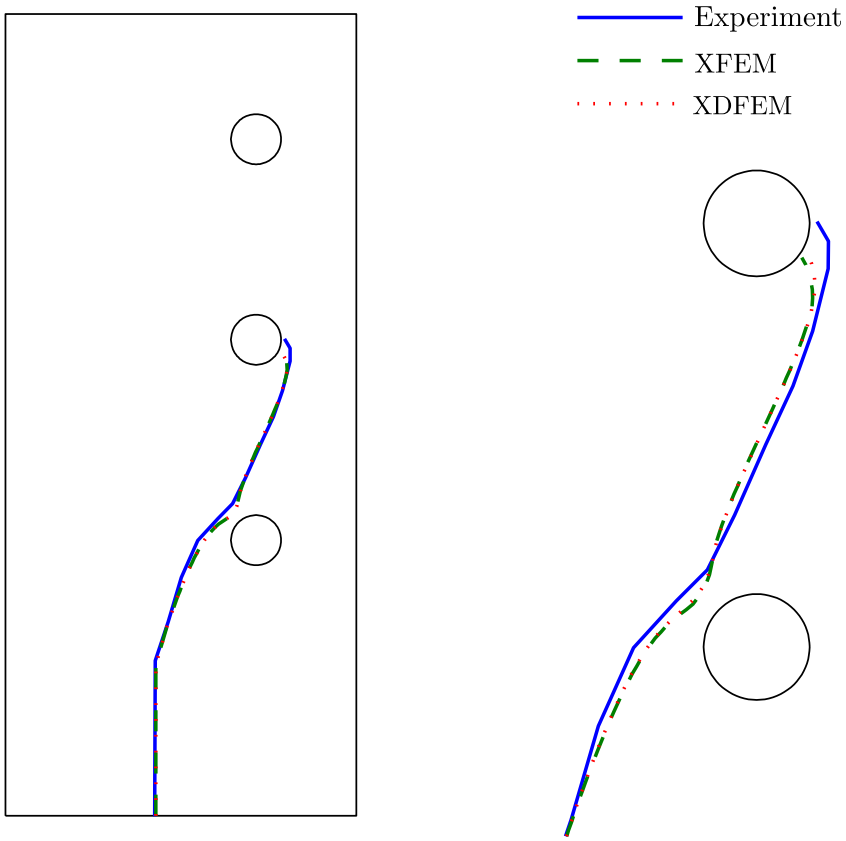

(a)

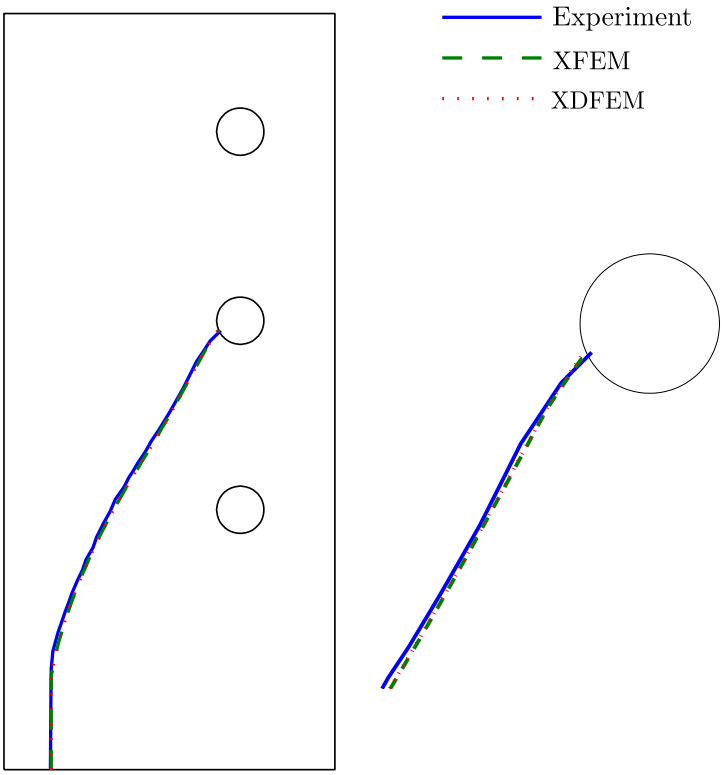

(b)

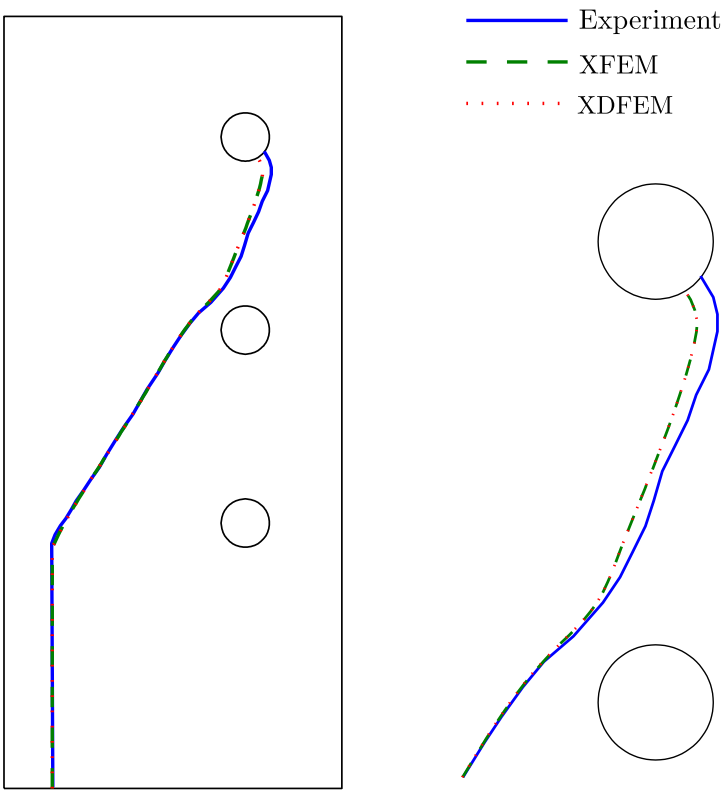

(c)

Figure 29: Crack evolution of the three cases

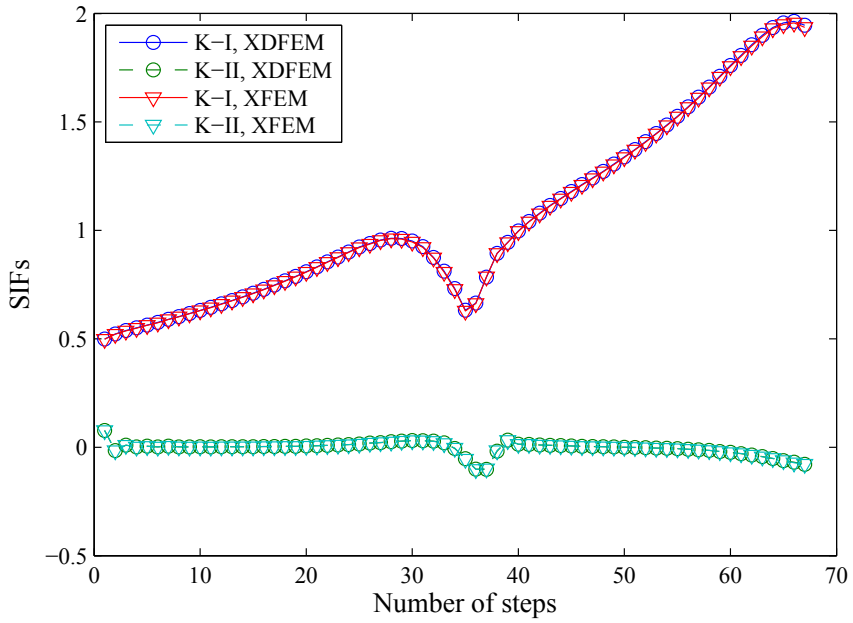
K−I, XDFEM
K−II, XDFEM
K−I, XFEM
K−II, XFEM
SIFs
Number of steps
2
1.5
1
0.5
0
−0.5
0
10
20
30
40
50
60
70

(a)

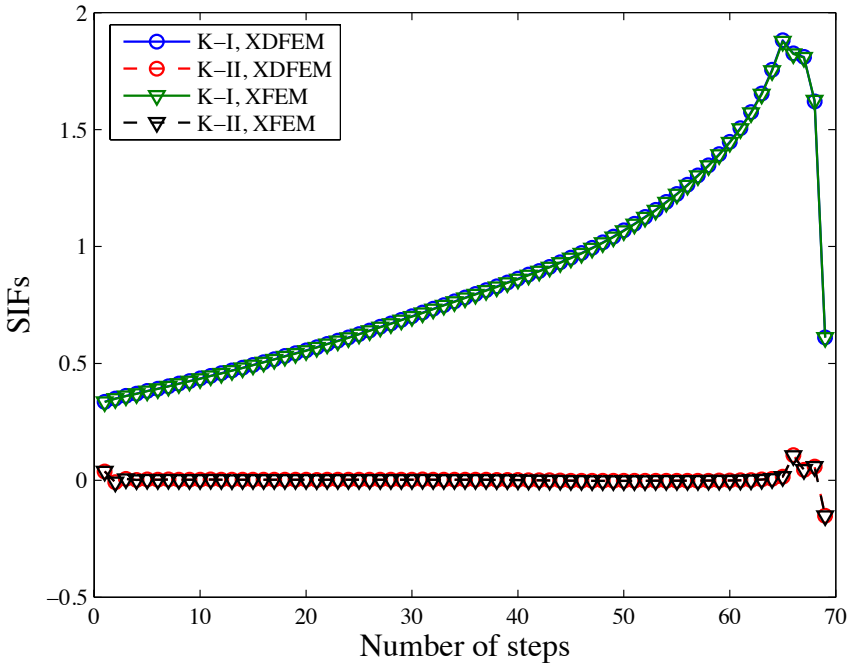
K−I, XDFEM
K−II, XDFEM
K−I, XFEM
K−II, XFEM
SIFs
Number of steps
2
1.5
1
0.5
0
−0.5
0
10
20
30
40
50
60
70

(b)

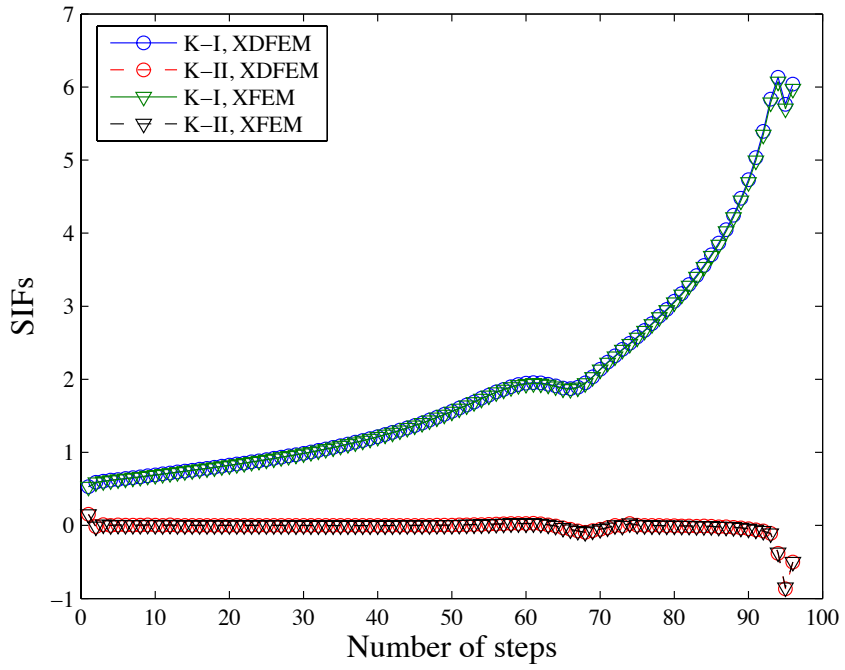

(c)

Figure 30: SIFs variation in three cases

5 Conclusion

This paper presented an enriched double-interpolation approximation method for linear elastic fracture and crack growth analysis. The double-interpolation approximation is constructed through two consequent stages of interpolation, i.e., the linear finite element interpolation for the first stage to produce an initial approximation field which will be utilized to reproduce the solution via a latter interpolation with smooth nodal gradients. Several examples are performed to explore and demonstrate the basic features of DFEM and XDFEM. The key points are summarized as follows:

- The precision of the solution field is almost improved by a level of $O(10^{-1})$ error in both displcement and energy norm without increasing the total DOFs, due to the fact that the basis functions of the double-interpolation approximation have been enhanced through the embedment of a kind of area weighted 'average' gradients. Numerical tests have shown that the double-interpolation method is even more accurate than the Q4 finite element in the same model size, despite of using the simplex mesh dicretization. It is well known that the quadrilateral (hexahadronal) mesh can achieve much better accuracy while, simplex mesh is more convenient to generate and has a strong adaptivity for using with arbitrary shape. DFEM proves to unite the two factors together to provide an practical and efficient modeling technique.

- The convergence rate of the DFEM is shown to behave like an intermediate of the linear finite element and quadratic finite element. The DFEM improves the accuracy based on the linear finite element mesh while decreases the DOFs if compared against quadratic finite element, which gives a comprise between the DOFs and precision in numerical modeling. In contrast to common higher-order finite element, DFEM owns the C^1 continuity on

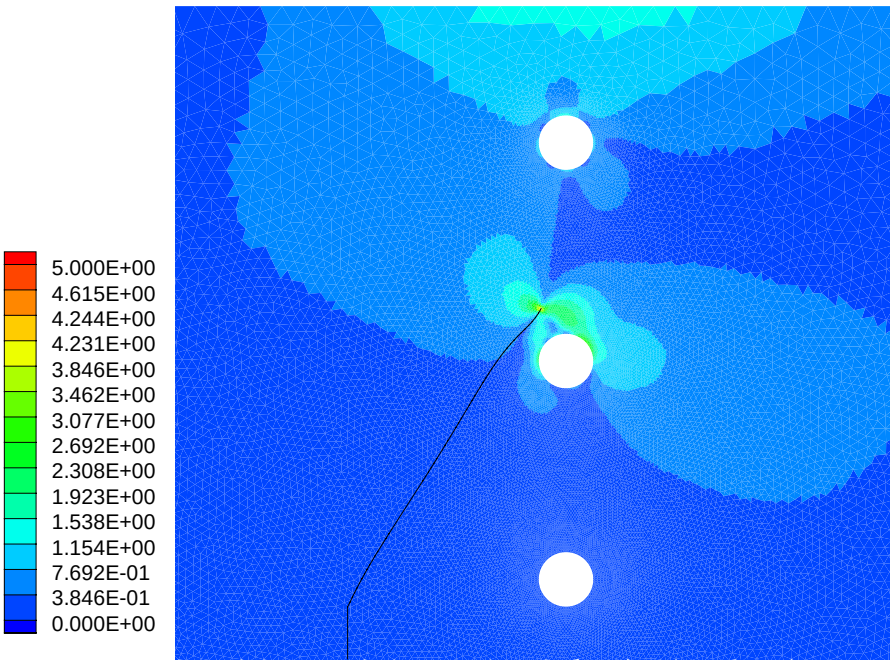

(a) XFEM, the 69th step

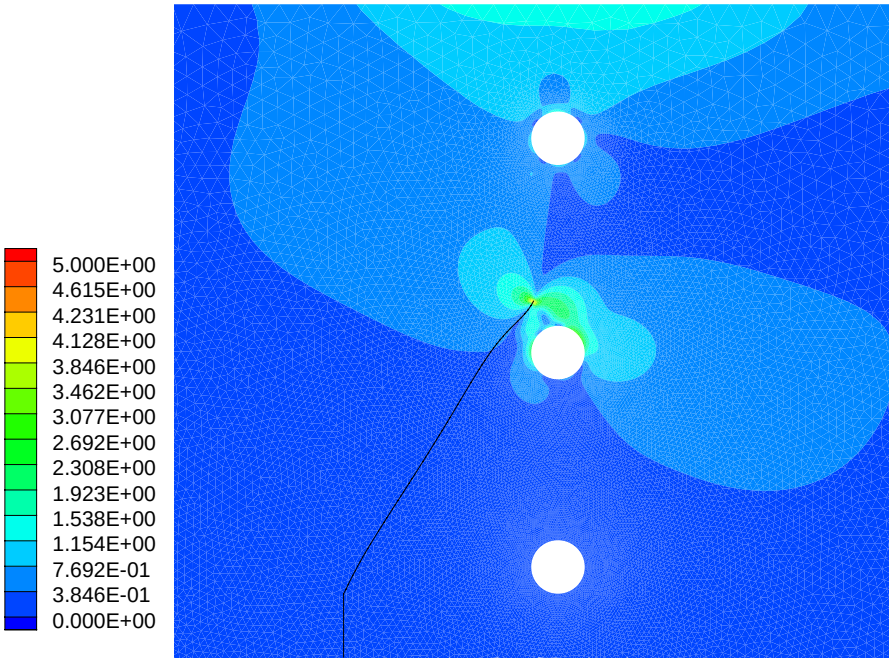

(b) XDFEM, the 69th step

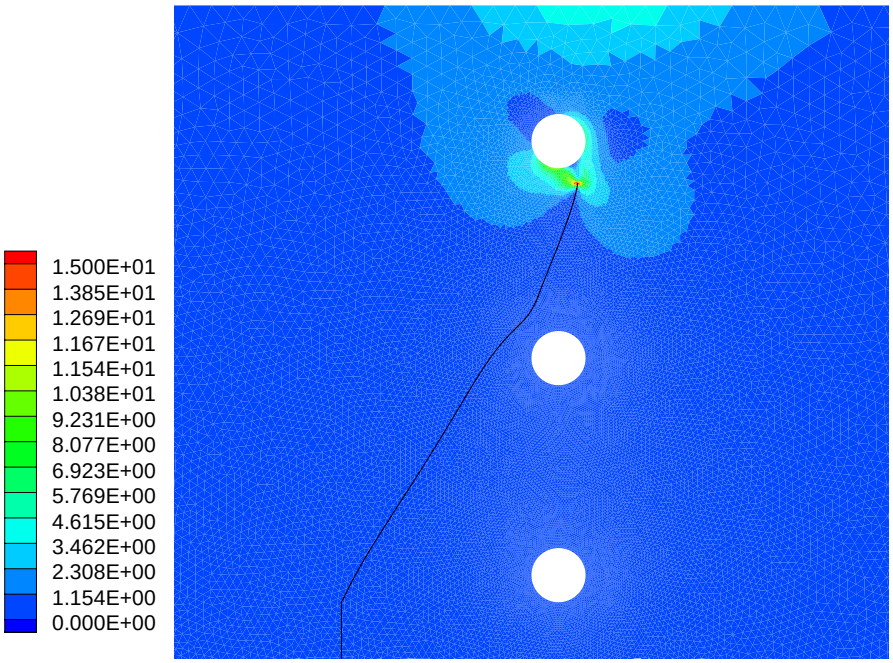

(c) XFEM, the 94th step

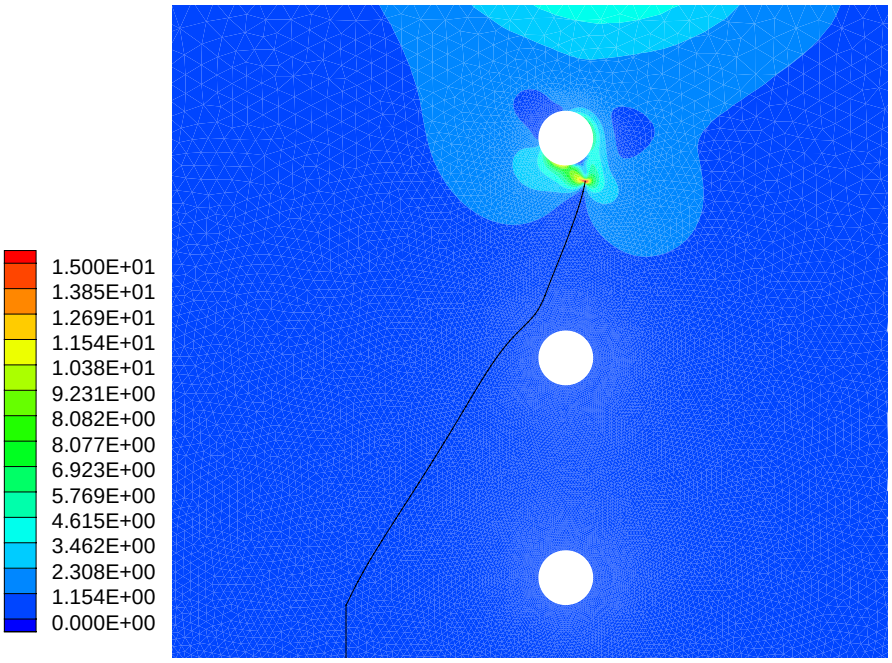

(d) XDFEM, the 94th step

Figure 31: Contour plots of Von Mises stress in case 3

most nodes. For continuum mechanics problems, it does not require any post-processing for recovering the nodal stress. For fracture analysis, only the topological enriched nodes need extra post-processing. Post-processing procedure is almost omitted in DFEM and XDFEM, which improves the efficiency of the simulation and maintains all the variables in the same space.

- It should be highlighted that the major factor which hampers the efficiency of DFEM is the increased bandwidth issue which is caused by the introduction of the average gradients. When the element-by-element strategy is used, the extra time needed in searching the stiffness matrix because of the expanded bandwidth can be saved.
- The XDFEM provide a robust application in crack propagation problems analogous to XFEM, whilst with a smoother stress field generated for evaluation. This could be more useful in improving the accuracy in 3D fracture modeling, in which the precision of Lagrange-based XFEM is poor due to the low continuity of the solution.

For the future work, the 3D XDFEM should be investigated to verify the accuracy of the solution with more practical implementation such as the preconditioning technique and element-by-element storage. The error estimation based on XDFEM is also an interesting topic for investigation. Further it would be beneficial to identify a procedure to maintain C^1 continuity at the topological enriched nodes. To further analyze the advantageous of XDFEM, detailed comparison should be made between XDFEM and the popular smoothed XFEM in terms of precision, stability and efficiency.

Acknowledgements

The authors would like to acknowledge the financial support of the Framework Programme 7 Initial Training Network Funding under grant number 289361 "Integrating Numerical Simulation and Geometric Design Technology" (FP7:ITN-INSIST).

References

[1] N Moës, J Dolbow, and T Belytschko. A finite element method for crack growth without remeshing. *International Journal for Numerical Methods in Engineering*, 46(1):131–150, 1999.

[2] J M Melenk and I Babuška. The partition of unity finite element method: Basic theory and applications. *Computer Methods in Applied Mechanics and Engineering*, 139(1-4):289–314, 1996.

[3] N Moës, A Gravouil, and T Belytschko. Non-planar 3D crack growth by the extended finite element and level sets-Part I: Mechanical model. *International Journal for Numerical Methods in Engineering*, 53(11):2549–2568, 2002.

[4] A Gravouil, N Moës, and T Belytschko. Non-planar 3D crack growth by the extended finite element and level sets-Part II: Level set update. *International Journal for Numerical Methods in Engineering*, 53(11):2569–2586, 2002.

[5] N Sukumar, D L Chopp, E Béchet, and N Moës. Three-dimensional non-planar crack growth by a coupled extended finite element and fast marching method. *International Journal for Numerical Methods in Engineering*, 76(5):727–748, 2008.

[6] G Zi and T Belytschko. New crack-tip elements for XFEM and applications to cohesive cracks. *International Journal for Numerical Methods in Engineering*, 57(15):2221–2240, 2003.

[7] P M A Areias and T Belytschko. Non-linear analysis of shells with arbitrary evolving cracks using XFEM. *International Journal for Numerical Methods in Engineering*, 62(3):384–415, 2005.

[8] T Belytschko, H Chen, J Xu, and G Zi. Dynamic crack propagation based on loss of hyperbolicity and a new discontinuous enrichment. *International Journal for Numerical Methods in Engineering*, 58(12):1873–1905, 2003.

[9] S Bordas and B Moran. Enriched finite elements and level sets for damage tolerance assessment of complex structures. *Engineering Fracture Mechanics*, 73(9):1176–1201, 2006.

[10] M Duflot and S P A Bordas. A posteriori error estimation for extended finite elements by an extended global recovery. *International Journal for Numerical Methods in Engineering*, 76(8):1123–1138, 2008.

[11] S P A Bordas and M Duflot. Derivative recovery and a posteriori error estimate for extended finite elements. *Computer Methods in Applied Mechanics and Engineering*, 196(35-36):3381–3399, 2007.

[12] S Bordas, P V Nguyen, C Dunant, A Guidoum, and H Nguyen-Dang. An extended finite element library. *International Journal for Numerical Methods in Engineering*, 71(6):703–732, 2007.

[13] E Wyart, M Duflot, D Coulon, P Martiny, T Pardoen, J.-F. Remacle, and F Lani. Substructuring FE–XFE approaches applied to three-dimensional crack propagation. *Journal of Computational and Applied Mathematics*, 215(2):626–638, 2008.

[14] J Shi, D L Chopp, J Lua, N Sukumar, and T Belytschko. Abaqus implementation of extended finite element method using a level set representation for three-dimensional fatigue crack growth and life predictions. *Engineering Fracture Mechanics*, 77(14):2840–2863, 2010.

[15] C A Duarte, O N Hamzeh, T J Liszka, and W W Tworzydlo. A generalized finite element method for the simulation of three-dimensional dynamic crack propagation. *Computer Methods in Applied Mechanics and Engineering*, 190(15–17):2227–2262, 2001.

[16] J Chessa, H Wang, and T Belytschko. On the construction of blending elements for local partition of unity enriched finite elements. *International Journal for Numerical Methods in Engineering*, 57(7):1015–1038, 2003.

[17] J E Tarancón, A Vercher, E Giner, and F J Fuenmayor. Enhanced blending elements for XFEM applied to linear elastic fracture mechanics. *International Journal for Numerical Methods in Engineering*, 77(1):126–148, 2009.

[18] R Gracie, H Wang, and T Belytschko. Blending in the extended finite element method by discontinuous Galerkin and assumed strain methods. *International Journal for Numerical Methods in Engineering*, 74(11):1645–1669, 2008.

[19] T Fries. A corrected XFEM approximation without problems in blending elements. *International Journal for Numerical Methods in Engineering*, 75(5):503–532, 2008.

[20] G Ventura, R Gracie, and T Belytschko. Fast integration and weight function blending in the extended finite element method. *International Journal for Numerical Methods in Engineering*, 77(1):1–29, 2009.

[21] G Ventura. On the elimination of quadrature subcells for discontinuous functions in the eXtended Finite-Element Method. *International Journal for Numerical Methods in Engineering*, 66(5):761–795, 2006.

[22] S Natarajan, D R Mahapatra, and S P A Bordas. Integrating strong and weak discontinuities without integration subcells and example applications in an XFEM/GFEM framework. *International Journal for Numerical Methods in Engineering*, 83(3):269–294, 2010.

[23] L Chen, T Rabczuk, S P A Bordas, G R Liu, K Y Zeng, and P Kerfriden. Extended finite element method with edge-based strain smoothing (ESm-XFEM) for linear elastic crack growth. *Computer Methods in Applied Mechanics and Engineering*, 209-212:250–265, February 2012.

[24] P Laborde, J Pommier, Y Renard, and M Salaün. High-order extended finite element method for cracked domains. *International Journal for Numerical Methods in Engineering*, 64(3):354–381, 2005.

[25] E Béchet, H Minnebo, N Moës, and B Burgardt. Improved implementation and robustness study of the X-FEM for stress analysis around cracks. *International Journal for Numerical Methods in Engineering*, 64(8):1033–1056, 2005.

[26] A Menk and S P A Bordas. A robust preconditioning technique for the extended finite element method. *International Journal for Numerical Methods in Engineering*, 85(13):1609–1632, 2011.

[27] N A Fleck and J W Hutchinson. Strain Gradient Plasticity. *Advances in Applied Mechanics*, 33(C):295–361, 1997.

[28] P Krysl and T Belytschko. Analysis of thin shells by the Element-Free Galerkin method. *International Journal of Solids and Structures*, 33(20–22):3057–3080, 1996.

[29] G Engel, K Garikipati, T J R Hughes, M G Larson, L Mazzei, and R L Taylor. Continuous/discontinuous finite element approximations of fourth-order elliptic problems in structural and continuum mechanics with applications to thin beams and plates, and strain gradient elasticity. *Computer Methods in Applied Mechanics and Engineering*, 191(34):3669–3750, 2002.

[30] S A Papanicolopulos and A Zervos. A method for creating a class of triangular C 1 finite elements. *International Journal for Numerical Methods in Engineering*, 89(11):1437–1450, 2012.

[31] S A Papanicolopulos and A Zervos. Polynomial C1 shape functions on the triangle. *Computers & Structures*, 118(0):53–58, 2013.

[32] P Fischer, J Mergheim, and P Steinmann. On the C1 continuous discretization of nonlinear gradient elasticity: A comparison of NEM and FEM based on Bernstein–Bézier patches. *International Journal for Numerical Methods in Engineering*, 82(10):1282–1307, 2010.

[33] T Belytschko, Y Y Lu, and L Gu. Element-free Galerkin methods. *International Journal for Numerical Methods in Engineering*, 37(2):229–256, 1994.

[34] W K Liu, S Jun, and Y F Zhang. Reproducing kernel particle methods. *International Journal for Numerical Methods in Fluids*, 20(8-9):1081–1106, 1995.

[35] K M Liew, X L Chen, and J N Reddy. Mesh-free radial basis function method for buckling analysis of non-uniformly loaded arbitrarily shaped shear deformable plates. *Computer Methods in Applied Mechanics and Engineering*, 193(3-5):205–224, January 2004.

[36] J G Wang and G R Liu. On the optimal shape parameters of radial basis functions used for 2-D meshless methods. *Computer Methods in Applied Mechanics and Engineering*, 191(23-24):2611–2630, 2002.

[37] G R Liu, G Y Zhang, Y T Gu, and Y Y Wang. A meshfree radial point interpolation method (RPIM) for three-dimensional solids. *Computational Mechanics*, 36(6):421–430, August 2005.

[38] M Arroyo and M Ortiz. Local maximum-entropy approximation schemes: a seamless bridge between finite elements and meshfree methods. *International Journal for Numerical Methods in Engineering*, 65(13):2167–2202, 2006.

[39] A Rosolen, D Millán, and M Arroyo. On the optimum support size in meshfree methods: A variational adaptivity approach with maximum-entropy approximants. *International Journal for Numerical Methods in Engineering*, 82(7):868–895, 2010.

[40] G R Liu. A generalized gradient smoothing technique and the smoothed bilinear form for Galerkin formulation of a wide class of computational methods. *International Journal of Computational Methods*, 05(02):199–236, 2008.

[41] S P A Bordas, T Rabczuk, H Nguyen-Xuan, V P Nguyen, S Natarajan, T. Bog, D. M. Quan, and N. V. Hiep. Strain smoothing in FEM and XFEM. *Computers & Structures*, 88(23-24):1419–1443, December 2010.

[42] G R Liu, L Chen, T Nguyen-Thoi, K Y Zeng, and G Y Zhang. A novel singular node-based smoothed finite element method (NS-FEM) for upper bound solutions of fracture problems. *International Journal for Numerical Methods in Engineering*, 83(11):1466–1497, 2010.

[43] N Vu-Bac, H Nguyen-Xuan, L Chen, S Bordas, P Kerfriden, R N Simpson, G R Liu, and T Rabczuk. A Node-Based Smoothed eXtended Finite Element Method (NS-XFEM) for Fracture Analysis. *Computer Modeling in Engineering & Sciences*, 73(4):331–356, 2011.

[44] Y Jiang, T E Tay, L Chen, and X S Sun. An edge-based smoothed XFEM for fracture in composite materials. *International Journal of Fracture*, 179(1-2):179–199, 2013.

[45] S P A Bordas and S Natarajan. On the performance of strain smoothing for quadratic and enriched finite element approximations (XFEM/GFEM/PUFEM). *International Journal for Numerical Methods in Engineering*, 86(4-5):637–666, 2011.

[46] S P A Bordas, T Rabczuk, and G Zi. Three-dimensional crack initiation, propagation, branching and junction in non-linear materials by an extended meshfree method without asymptotic enrichment. *Engineering Fracture Mechanics*, 75(5):943–960, 2008.

[47] C Zheng, S C Wu, X H Tang, and J H Zhang. A novel twice-interpolation finite element method for solid mechanics problems. *Acta Mechanica Sinica*, 26(2):265–278, June 2009.

[48] S C Wu, W H Zhang, X Peng, and B R Miao. A twice-interpolation finite element method (TFEM) for crack propagation problems. *International Journal of Computational Methods*, 09(04):1250055, 2012.

[49] S Timoshenko and J N Goodier. *Theory of Elasticity*. Engineering societies monographs. McGraw Hill Book Company, 1972.

[50] H M Westergaard. Bearing pressures and cracks. *Journal of Applied Mechanics*, 6:A49–A53, 1939.

[51] A R Ingraffea and M Grigoriu. Probabilistic fracture mechanics: A validation of predictive capability. *Department of Structure Engineering, Cornell University*, Rep. 90-8, 1990.

[52] T N Bittencourt, P A Wawrzynek, A R Ingraffea, and J L Sousa. Quasi-automatic simulation of crack propagation for 2D LEFM problems. *Engineering Fracture Mechanics*, 55(2):321–334, 1996.

[53] G Ventura, J X Xu, and T Belytschko. A vector level set method and new discontinuity approximations for crack growth by EFG. *International Journal for Numerical Methods in Engineering*, 54(6):923–944, 2002.